Science of the Total Environment 907 (2024) 167934

Contents lists available at ScienceDirect

Science of the Total Environment

journal homepage: www.elsevier.com/locate/scitotenv

Compound drought and heat waves variation and association with SST modes across China

Xiaolong Pan [a,b], Weiguang Wang [a,b,*], Quanxi Shao [c], Jia Wei [a,b,*], Hongbin Li [a,b], Fengyan Zhang [b], Mingzhu Cao [a,b], Liyan Yang [a,b]

[a] The National Key Laboratory of Water Disaster Prevention, Hohai University, Nanjing 210098, China
[b] College of Hydrology and Water Resources, Hohai University, Nanjing 210098, China
[c] CSIRO Data 61, Australian Resources Research Centre, Bentley, WA, Australia

HIGHLIGHTS

- A new identification framework is used to evaluate compound drought and heat waves (CDH).
- CDH characteristics averaged over China increased dramatically since 1990s.
- Mild CDH events are more susceptible to SST anomalies variations than severe ones.
- IOD dominates in intensifying CDH in the northwest and north regions.

GRAPHICAL ABSTRACT

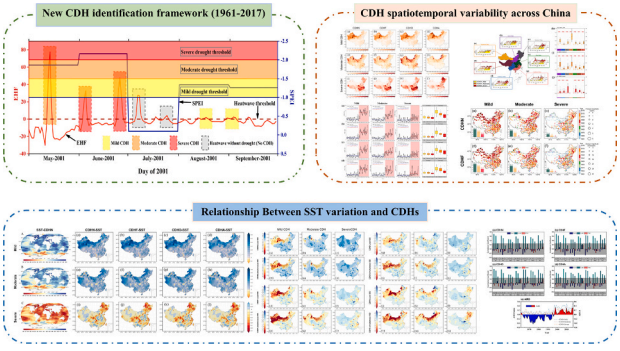

ARTICLE INFO

Editor: Fernando A.L. Pacheco

Keywords:
Drought
Heat wave
Compound event
Sea surface temperature modes
ENSO
IOD

ABSTRACT

Compound drought and heatwaves (CDH) have garnered increasing attention because concurrent extreme events can exacerbate the harmful impacts caused by univariate extremes. However, various severities in CDH events and their relationships with sea surface temperature (SST) variations in China remain little understood. Here, we accurately identify CDH events and multi-aspect of characteristics using the standardized precipitation evapotranspiration index (SPEI) and the excess heat factor (EHF) during the extended summer (May–September) of 1961–2017. The evolution of multifaceted characteristics of CDH and their association with SST variation are further explored. The results suggest that the number, frequency, duration and intensity of regional CDH events show heterogeneous spatial patterns, with a significant increasing trend. A consistent abrupt transition in CDH characteristics averaged over China occurred in the period of 1993–1996. Mild and moderate CDHs occur more commonly in Northwest and North China, whereas severe CDHs are mainly found in central and eastern regions. Mild and moderate CDHs are more susceptible to SST modes than severe CDH, and there are strong positive correlations between mild and moderate CDH characteristics and SST variations in the northwest and northern regions. Compared to El Niño-Southern Oscillation (ENSO), Indian Ocean Dipole (IOD) plays a dominant role in the intensifications of mild and moderate CDH events. Regionally, the northwest and north have experienced longer, more frequent and severe CDH events during the positive phase of IOD. These findings reveal the

* Corresponding authors at: The National Key Laboratory of Water Disaster Prevention, Hohai University, Nanjing 210098, China.
E-mail addresses: wangweiguang@hhu.edu.cn (W. Wang), wj_227@126.com (J. Wei).

https://doi.org/10.1016/j.scitotenv.2023.167934
Received 15 August 2023; Received in revised form 5 October 2023; Accepted 17 October 2023
Available online 18 October 2023

divergent evolutions in CDH characteristics with various severities and inconsistent impacts of different SST modes on the compound events.

1. Introduction

With climate warming, the harmful effects of the combination of extreme climate events, like droughts and heat waves, cannot be overlooked. The continued increase and proliferation of compound droughts and heat waves (CDH) have raised widespread concerns in recent years (e.g., Fink et al., 2004; Sharma and Mujumdar, 2017; Sutanto et al., 2020; Zscheischler et al., 2018). Heat waves and droughts, both highly destructive natural hazards, can cause significantly more harm to water supplies, agriculture, ecosystems, socioeconomic activity, and human health when they occur simultaneously than single-hazard occurrences. (Allen et al., 2010; Bandyopadhyay et al., 2012; Mishra et al., 2020; Mukherjee et al., 2020; Perkins et al., 2012; Shukla et al., 2015). For example, in the summer of 2010, Europe and western Russia suffered unprecedented heat waves (Barriopedro et al., 2011), accompanied by droughts triggered by less precipitation and hot air (Hauser et al., 2016; Witte et al., 2011), resulting in human deaths and severe decrease in Russian food output (Grumm, 2011). Similarly, the Yangtze River basin in China experienced record-breaking heat wave in the summer of 2022, and the persistent exceeding heat led to a severe drought with negative impacts rippling through agriculture, hydropower, and other industries (Hua et al., 2023; Ma and Yuan, 2023). Therefore, accurate identification of CDH as well as their severity is critical.

Drought as one of the most catastrophic natural hazards affects surface and groundwater resources and has substantial impacts on agricultural productivity, natural ecosystems, and socio-economic activities (Cheng et al., 2022; Duan et al., 2021; Feng et al., 2019). Meanwhile, alarming heat waves have occurred over the world in recent decades as global temperatures have risen (Coumou and Rahmstorf, 2012). Previous study explored substantial increases of concurrent heat waves and drought events in America during the period of 1960 to 2010, although no significant increases in single heat wave and single drought events (Mazdiyasni and AghaKouchak, 2015). There is a statistical association or reliance between the factors that cause dryness and heat waves (Alizadeh et al., 2020; Chiang et al., 2018; Leonard et al., 2014). Recent studies demonstrated that the stronger the negative association between precipitation and temperature is, the more frequently concomitant occurrences of heat waves and drought are (Zscheischler and Seneviratne, 2017). Furthermore, anomalies in local meteorological conditions are the physical preconditions for the onset of CDH, as heatwaves can lead to the spread and exacerbation of droughts through soil-precipitation feedbacks (Miralles et al., 2019).

The drivers of such extreme compound events by large scale meteorological factors deserve further study. For example, atmospheric blocking (Rex, 1950) is closely linked to extreme climate events. When atmospheric blocking occurs in the summer, it can cause heat waves, droughts or floods (Dong et al., 2018), and both the El Niño-Southern Oscillation (ENSO) and the Pacific Decadal Oscillation (PDO) influence the intensity of blocking (Barriopedro et al., 2006; De Adana and Colucci, 2005; Renwick, 1998). Furthermore, the current understanding of the physical mechanisms underlying droughts and heat waves reveals that, while droughts tend to develop longer than the heat waves, both are driven by persistent large-scale circulation anomalies as crucial features (Quesada et al., 2012; Rowell, 2009; Seager and Hoerling, 2014; Vautard et al., 2007), which partly explains why these two extreme events frequently occur together.

Although the occurrence of drought and heat waves at the same time is characterized as a compound event, there is less agreement on how to describe the single drought and single heat waves within this concurrent condition. Previous researches have examined variations in the CDH events using precipitation deficiencies, temperature anomalies, and other pertinent variables (e.g., Hao et al., 2018a; Kong et al., 2020; Lu et al., 2018; Manning et al., 2018; Mazdiyasni and AghaKouchak, 2015). However, given the differences in drought and heat waves time scales, as well as the differences in feedback mechanisms between drought and heat waves across regions, it is critical to develop more appropriate drought and heat waves indices based on regional climatic factors (Mukherjee et al., 2020). Given the variety of climate in different places, the relative threshold definition may be more appropriate for describing heat waves. Temperature is not only used to quantify heat waves, but also plays a key role in the drought genesis mechanism (Dai and Zhao, 2017). As a result, when recognizing compound drought and heat waves events, it would be more meaningful to utilize drought indices that take temperature into account to define drought (Feng et al., 2021). Furthermore, accurately categorizing the severity of CDH is essential for determining their adverse consequences (e.g., Mazdiyasni and AghaKouchak, 2015; Wu et al., 2019a), as the destructive effects of extreme compound events are more deadly than common events for food crises and human health.

Sea surface temperature (SST) anomalies have had complicated environmental consequences under global warming and are important to the onset of catastrophic climatic events. Nonetheless, the understanding of how SST modes affect CDH is still limited. The major phase of tropical ocean variability is the ENSO, whose anomalous fluctuations have considerable impacts on large-scale circulation evolution and regional climate conditions, causing many extreme natural hazards (Barlow et al., 2001; Bouma et al., 1997; Kogan, 2000). SST changes, particularly ENSO and Indian Ocean Dipole (IOD), have been linked to high temperature and droughts in previous studies (Seager and Hoerling, 2014), and ENSO in particular influences the onset of summertime CDH events in the tropics (Hao et al., 2018b). Other large-scale SST modes like PDO and North Atlantic Oscillation (NAO) may affect the onset of CDH events independently or in conjunction with ENSO and IOD, which may reinforce or diminish their effects (Chang et al., 2006; Saji and Yamagata, 2003). With the influence of global warming, the dominant SST modes are in constant change in their background conditions and dynamical systems, with complex and variable intensity, frequency, and phase transitions. Recent researches suggest that SST mode in different periods or phases can have conflicting results. The lead ENSO have a substantial influence on temperature by magnifying the vapor feedback, but the simultaneous ENSO generate more durable and powerful heat waves by modifying circulation patterns (Murari et al., 2016; Oueslati et al., 2017; Wei et al., 2020). Moreover, the dominant SST mode that determines the variability of CDH in different regions remains ambiguous (Parker et al., 2014; Perkins et al., 2015). More studies into the impacts of the SST modes and their consequences during different periods and phases are required (Wei et al., 2020). Contrary to ENSO and IOD, which have interannual cycles, Atlantic Multi-decadal Oscillation (AMO), PDO, and NAO have decades-long cycles and can be in one phase for several years, preventing them from capturing the variations of CDH response to SST modes in different periods of the year. Therefore, this research is more interested in exploring the impact of ENSO and IOD, which are more influential on climate in China, on CDH during different periods.

China locates in the East Asian monsoon region, which has a high rate of environmental change on Earth (Ding and Qian, 2011). It also possesses the world's third largest agricultural arable land area. The complexity and importance of investigating extreme compound events in China are heightened by the complex and various climate types. Compound drought and heat waves have been on the rise in China over an extensive area (Li et al., 2020; Li et al., 2019; Wu et al., 2019b; Ye et al., 2019; Zhou and Liu, 2018), which created massive multiple

pressures on agriculture and ecosystems, such as the summer of 2006 in southwest China and the summer of 2013 in southern China, where compound drought and heat waves caused massive direct and indirect economical loss (Lu et al., 2018; Yuan et al., 2016). However, there are few in-depth studies in China that examine the regional and temporal evolution and driving factors of compound droughts and heat waves. Large-scale ocean-atmosphere variability patterns have linked to a variety of extreme events and climatic variabilities around the world (Sun et al., 2016a; Sun et al., 2016b; Wu et al., 2021a; Yang et al., 2017). SST anomalies have substantial influences on precipitation and temperature changes in China because they trigger the anomalous climatic situations and related dynamics such as sustained anticyclonic and vapor feedbacks (Wei et al., 2020). However, existing knowledge of the various SST patterns as drivers is founded primarily on individual localities rather than quantitative systematic studies over China (Wei et al., 2020). Therefore, there is a growing need to accurately identify and investigate compound droughts and heat waves in vulnerable regions utilizing appropriate indicators, as well as to explore the response of compound events of varying severity to SST modes across different regions.

In this study, we use an integrated identification methodology that integrates drought and heat waves. Using EHF and SPEI metrics, we examined the spatial and temporal characteristics of multiple aspects of the number, frequency, duration, and intensity of CDH events across China during the period of 1961–2017. The relationships between global SST change and CDH characteristics of varying severity, as well as the influence of different ENSO and IOD phase (lead and simultaneous), are investigated. The responses of compound events of varying severity to ENSO and IOD are also scrutinized.

2. Study area and data sources

2.1. Study area

China covers a vast area and is affected by the monsoon over a large area (Fig. 1). The regional distributions of annual mean temperature and precipitation vary substantially due to the broad span of latitude and longitude, complicated topography, and various vegetation, resulting in diverse climatic features (Wu et al., 2019a). Average summer temperatures in the eastern regions have risen by 0.82 °C over the last six decades (Sun et al., 2014), whereas hotter summers have grown more frequent in the northern (Kang and Eltahir, 2018; Zhang et al., 2015). With the influence of climate warming and human activities and other factors, drought in China has expanded in scope and intensified in severity (Lin et al., 2015). Meanwhile, as the population ages, severe heat waves endanger the health of a growing number of individuals, and heat-related deaths in China have skyrocketed (Bai et al., 2014; Zhang et al., 2018).

2.2. Data sources

Precipitation, wind speed, relative humidity, sunshine duration, and daily maximum and minimum temperatures were derived from the China Meteorological Administration's National Meteorological Information Center (http://www.tpdc.ac.cn/en/data/52c77e9c-df4a-4e27-8e97-d363fdfce10a/). Meteorological stations with >3 days of missing data were excluded. The 725 stations shown in Fig. 1 were employed.

The two major climatic models affecting Asian climate, ENSO and IOD, are investigated in this paper. Monthly global SST is NOAA Extended Reconstructed SST V5 at 2° × 2° resolution (Huang et al., 2017). The monthly multivariate ENSO index (MEI) and dipole mode index (DMI) are obtained from https://www.esrl.noaa.gov/psd.

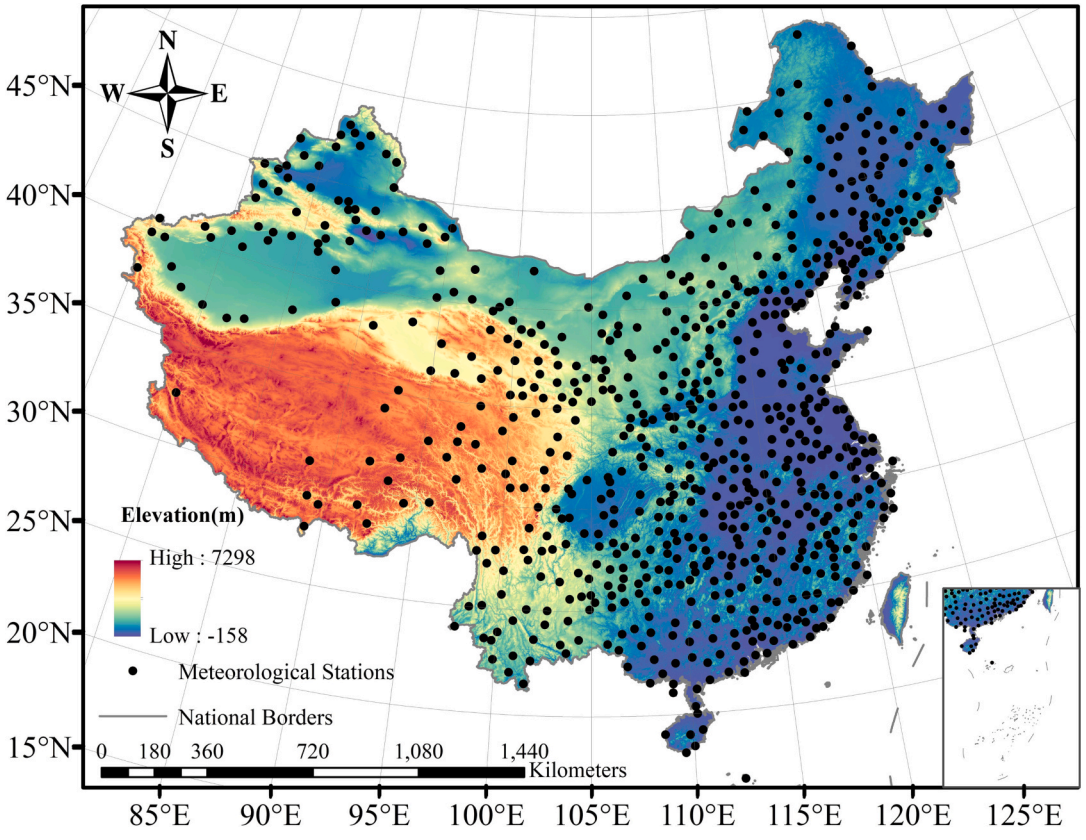

Fig. 1. The study area and the locations of the 725 meteorological stations used.

Monthly global SST of the NOAA Extended Reconstructed SST V5 is available at https://www.esrl.noaa.gov/psd/data/gridded/data.noaa.ersst.v5.html. The simultaneous phases of ENSO and IOD are derived from calculating monthly averages from May to September (CDH study period). We chose December–February (denoted by 0) for ENSO and September–November (denoted by 0) for IOD as the lead phases, because they generally peak during the two periods (Hong et al., 2010; Hong et al., 2008; Liu et al., 2015; Wei et al., 2019). Furthermore, monthly sea-level pressure, geopotential height, and cloud cover were obtained from the NCEP-NCAR reanalysis product (https://www.esrl.noaa.gov/psd/data/gridded/data.ncep.reanalysis.html), with a 2.5° × 2.5° resolution.

3. Methodology

3.1. Defining compound drought and heat waves (CDH) events

3.1.1. Heat wave metrics: EHF

In this study, we characterize heat waves using the excess heat factor (EHF) derived from the daily max and min surface air temperatures. The definition of EHF was proposed in 2009 by Nairn et al. (2009). Compared with past heat waves indicators, the EHF has two advantages. One is that the calculation process incorporates both daytime and nocturnal heat conditions into the single indicator, allowing for the past phenomena of considerable overnight temperature increase to be taken into consideration. The other is the incorporation of local pre-heat accumulation conditions, as pre-heat accumulation conditions can either enhance or weaken heat changes. This approach has been intensively tested for reliable detection of heat wave events and more accurate representation of heat waves intensity (Nairn et al., 2018; Nairn and Fawcett, 2015; Perkins and Alexander, 2013). The EHF includes two elements, the significance index (EHI_{sig}) and the acclimatization index (EHI_{accl}), which are expressed as follows:

$$EHI_{sig} = \frac{(T_i + T_{i-1} + T_{i-2})}{3} - T_{95} \quad (1)$$

and:

$$EHI_{accl} = \frac{T_i + T_{i-1} + T_{i-2}}{3} - (T_{i-3} + \ldots + T_{i-32}) \Big/ 30 \quad (2)$$

where T_i is the daily mean temperature for day i, and T_{95} is the 95th percentile of the daily mean temperature (T_i) for the 1961–1990 climate reference period. The daily mean temperature is calculated from 1 May to 30 September during 1961–2017, defined as $T_i = (T_{max} + T_{\min})/2$, where T_{max} (T_{min}) is the maximum (minimum) temperature within a 24-h cycle (0900–0900 LT). The T_{95} is calculated for each station on a daily basis within a 15-day window centered on T_i. Day i is in °C for T_i, and the units of EHI_{sig} and EHI_{accl} are both °C.

EHI_{sig} depicts the anomaly of the 3-day window average temperature relative to the threshold (T_{95}), while EHI_{accl} describes the anomaly of the average temperature in the same window relative to the preceding 30 days. Lastly, combining Eqs. (1) and (2), the EHF is expressed as follows:

$$EHF = EHI_{sig} \times max(1, EHI_{accl}) \quad (3)$$

The unit of EHF is $°C^2$, this formula ensures that $sign(EHF) = sign(EHI_{sig})$.

3.1.2. Drought metrics: SPEI

The standardized precipitation evaporation index (SPEI) derived by calculating potential evapotranspiration (PET) using the Penman-Monteith (PM) equation was used to define drought events. The SPEI (Vicente-Serrano et al., 2010) based on precipitation and temperature data has the advantage of combining multi-scale features with consideration of the impact of temperature change on drought assessment. Common methods for calculating PET are the empirical temperature-based Thornthwaite equation (Thornthwaite, 1948), the PM equation, and the improved model 2S PET model based on the PM equation. However, previous studies have demonstrated that when the Thornthwaite equation is used to calculate PET, the impact of temperature change on drought features in the Chinese desert zone is typically magnified (Chen and Sun, 2015), neglecting other variables related to atmospheric water demand (Zhang et al., 2017b). The PM equation was proposed by Penman (1948) on the basis of fundamental physical principles, taking into account thermodynamic and aerodynamic effects. In addition, the SPEI obtained using the PM equation has a better response to the observational soil moisture and runoff changes of China and better reflects the climate change conditions in the region (Chen and Sun, 2015). The SPEI for 1961–2017 is calculated on 1-month time scale from 725 observatories covering China. Table 1 lists the SPEI-based criteria for dryness and wetness ratings.

3.1.3. CDH events and severity classification

A comprehensive temporal framework is employed in this paper to define, identify and classify CDH events (Fig. 2). Based on the indices mentioned above, we define heat wave events, drought events, and CDH in this section. The formal definition is as follows: firstly, a drought is an event that results in SPEI ≤ -1.0, i.e., a month with a SPEI ≤ -1.0 is a drought month. Secondly, a heat wave is an event that at least 3 consecutive days of warm conditions with EHF > 0. It is worth emphasizing that even multiple consecutive three days with EHF > 0 are still considered as a single heat wave event, unless there is a hiatus after which we would recalculate the heat wave event. Following that, a CDH event is defined as a heat wave event that happens during a drought event (e.g., Alizadeh et al., 2020; Mazdiyasni and AghaKouchak, 2015; Sharma and Mujumdar, 2017; Zscheischler et al., 2018). Specifically, there will be one or more CDH events when one or more heat wave events (EHF > 0) occurred within a drought period (SPEI ≤ -1.0). The calculation of SPEI (drought) includes temperature, the only element that defines a heat wave. Drought events at longer time scales (one month) have a dominant influence in sustaining the underlying surface and atmospheric conditions for the onset and development of heat waves on three-day scales (Barriopedro et al., 2011; Fischer et al., 2007; Quesada et al., 2012; Schumacher et al., 2019). The coupling between the EHF and SPEI also suggests that the more severe the drought (the smaller the threshold range of SPEI), the more likely to occur a heat wave (the higher the probability of EHF >0) over China (Fig. S1). Therefore, we classify the severity of CDH events according to the severity of the drought when it occurs concurrently with the heat waves. To be clear, our definition of CDH severity is a combination of drought and heat waves influencing factors and interactions, rather than considering drought alone. The CDH events are classified as mild (-1.5<SPEI ≤ -1.0), moderate (-2.0<SPEI ≤ -1.5), and severe (SPEI ≤ -2.0) (Wei et al., 2021), denoted as CDHMI, CDHMO, and CDHSE, respectively. Finally, for each station, the annual occurrence of various severity compound drought and heat waves events was calculated.

The expanded impact, incidence, and risk of CDH globally requires a clearer view of how it is changing (He et al., 2022). Previous researches have examined heat waves, droughts, and their compound events from different characteristic perspectives (He et al., 2022; Murari et al., 2016;

Table 1
Classification of wetness and dryness classes based on SPEI and corresponding cumulative probabilities.

Categories	Value	Cumulative probability (%)
Extremely wet	≥ 2.0	2.28
Severely wet	1.50–1.99	6.68
Moderately wet	1.00–1.49	15.87
Near normal	−0.99–0.99	50.00
Moderately dry	−1.49 to −1.00	84.13
Severely dry	−1.99 to −1.50	93.32
Extremely dry	≤−2.0	97.72

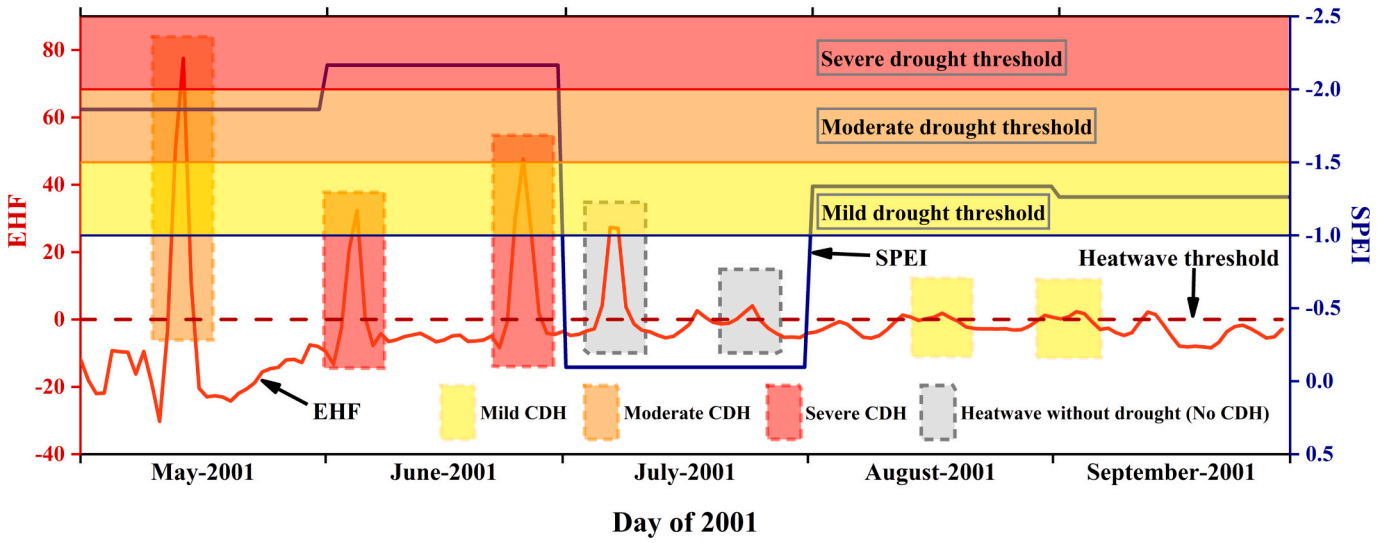

Fig. 2. A comprehensive framework for identifying and classifying CDH. The right y-axis represents SPEI and the left y-axis represents EHF.

Oueslati et al., 2017; Thomas et al., 2016; Wong et al., 2013). A multi-perspective features quantifying the number (CDHN), frequency (CDHF), longest duration (CDHD), and amplitude (CDHA) of CDH events is used (Table 2). CDHN is the total number of CDH events per year, CDHF is the total participating days of CDH events per year, CDHD is the longest duration of CDH events per year, and CDHA is the EHF peak magnitude of the hottest CDH events per year.

3.2. Regionalization of study area

In order to identify regional CDH change characteristics, the Fuzzy C-Mean (FCM) algorithm was used to partition the climate types in China (Zhang et al., 2017a, 2017b). The clustering partitioning in this paper takes 6 elements of temperature, precipitation, potential evapotranspiration, and corresponding station location longitude, latitude, and elevation as input variables for 725 stations. To effectively avoid data redundancy caused by autocorrelation among the input variables, the principal component analysis (PCA) was utilized to process the input variables and reduce the dimensionality of the input variables. The FCM clustering classification process is shown in Fig. S2. The cumulative variance explained of the first four principal components exceeded 95 % (supporting Table S1), so the first four principal components are selected as the input variables for FCM clustering in this study. Three validity indices were considered to determine the optimal number of subregions, namely fuzziness performance index (FPI), partition index (SC) and Extended Xie-Beni index (Xie-Beni) (supporting Fig. S2). Finally, seven subregions with similar climatic conditions were identified, named as North China (NC), Southwest China (SWC), Northeast China (NEC), Northwest China (NWC), East China (EC), West China (WC), and Southeast China (SEC) based on the geographic locations (supporting Fig. S3). The cluster partitioning results produced anomalies due to the special environment (e.g., higher altitude) of several stations, which contrasted with the climatic conditions of the surrounding area, with few stations (1.24 %) far from their corresponding subregions. The perturbations caused by such very few anomalous stations have almost no effect on the results after regional averaging (0.02 % - 6.51 %). The map shown in Fig. 5 shows the clustered partition map after optimizing the sub-region boundaries. The CDH characteristics of stations far from their corresponding subregions are counted in the subregion in which the station is geographically located.

Table 2
Indices of compound droughts and heat waves characteristics.

Indices	Definition	Unit
CDHN	Number of CDH	Number of events
CDHF	Frequency of CDH	Days
CDHD	Longest duration of CDH	Days
CDHA	Peak amplitude of heat waves in CDH	°C

3.3. Trend analysis and abrupt change point test methods

The Pettitt test (Pettitt, 1979) is a nonparametric test for identifying possible abrupt changes in a time series with the advantage of being computationally simple, less affected by outlier fluctuations, and more suitable for identifying the first abrupt change in a hydrometeorological series. The Pettitt test assumes that the data are independent and identically distributed, which is usually not applicable to meteorological data, since may exhibit serial dependency (Richardson et al., 2022). We applied a block bootstrap procedure (Kunsch, 1989; Lahiri, 2003; Wilks, 1997, 2019) with 10,000 replicates to mitigate the influences of autocorrelation. To consider spatial autocorrelation and multiple testing, we controlled the false discovery rate (FDR; Benjamini and Hochberg, 1995). The FDR method is effective in controlling the proportion of false rejection tests and is robust to spatial dependence. We set $\checkmark_{FDR} = 0.1$ (Wilks, 2016) permitting 10 % of statistically significant results to be wrong. For a complete technical description of these methods, please see the supporting materials.

3.4. Correlation between global SST and CDH

The widely utilized singular value decomposition (SVD) approach is used in this paper. SVD is extensively used to find the distantly associated statistical features between distinct variables because it can isolate the most essential anisotropic correlation modes of two variable fields (Bretherton et al., 1992). SVD has also been used in recent years to analyze the relationship between North and South American runoff and global SST (Tootle and Piechota, 2006; Tootle et al., 2008). Therefore, the correlation between global SST anomalies and CDH characteristics across China was investigated using the SVD method. Additionally, Pearson correlation was utilized as an aid to explore the correlation between CDH characteristics and ENSO, IOD index.

3.5. Modes of SST and composite analysis

MEI values derived from the full multivariate signals over the tropical Pacific are used in the ENSO measurement. The threshold of ±0.5 °C

was used to classify El Niño (>0.5), neutral, and La Niña (<−0.5) seasons. The lead mature and simultaneous phases of ENSO are December–February (0) and May–September (1), respectively. The DMI obtained from the Indian Ocean SST gradient anomalies between the western equator (50°E - 70°E and 10°S - 10°N) and the southeastern equator (90°E - 110°E and 10°S - 0°N) was used to calculate IOD. A threshold of half the standard deviation was used to distinguish between positive, neutral and negative seasons. The MEI ± 0.5 °C threshold used to classify ENSO as El Niño and La Niña has been widely applied for research in atmospheric and oceanic disciplines (Lee, 2015; Sang et al., 2019; Wei et al., 2020), as has the DMI for IOD (Lee, 2015; Sang et al., 2019; Wei et al., 2020). The lead mature and simultaneous phases of IOD are September–November (0) and May–September (1), respectively. Because ENSO and IOD often peak during these months, we chose DJF (0) and SON (0) as the lead mature phases. Table S2 depicts the lead and simultaneous seasons of ENSO and IOD phases. The effect of different phases of SST modes on CDH was analyzed within the lead and simultaneous periods. The standard *t*-test was employed to estimate statistical significance. The interpolation method used in this work is the Inverse Distance Weighting (IDW) interpolation. The weight function is a power function with weights proportional to the inverse distance to the power of 2, the output image size is defaulted to 0.14453, and the minimum number of points within the search radius is 12.

4. Results

4.1. CDH spatiotemporal variability over the last 57 years

4.1.1. The spatial pattern of CDHs

Fig. 3 shows the spatial distribution of multiyear averages of CDHN, CDHF, CDHD, and CDHA in China from 1961 to 2017. Most stations in the country had an annual average of no >0.3 mild, 0.2 moderate, and 0.1 severe CDH events. An average of 0.3–1.0 CDHMI occur each year in Northwest China and parts of North China. North China and areas of Northwest China have 0.2–0.6 CDHMO per year, while Xinjiang's Hami City (93°44′E, 42°78′N) can have 0.6–1 CDHMO per year, and Izhou District (93°31′E, 42°49′N) of Hami can have up to 1.7 times CDHMO per year. Further analysis revealed that the spatial pattern of CDHSE events is the inverse of CDHMI and CDHMO, with high CDHN values primarily distributed in Eastern China, Southwest China, Northeast China, and parts of West China, with 0.1–0.3 times CDHSE occurring on average per year in these regions. For three levels of CDH events, the spatial pattern of CDHF and CDHD is similar to that of CDHN. In general, the longest CDHMI lasted no >2 days throughout the year. In areas where moderate CDHN occurs >0.2 times, CDHF is higher than 1 day and CDHD can be >0.6 days. Notably, the CDHF of CDHMO in Hami, Xinjiang, reached 9.9 days on average, with the longest duration lasting >3 days. CDHF was >0.4 days and CDHD was >0.3 days in locations where severe CDHN occurred >0.1 times. The CDHF of CDHSE does not exceed 2 days in most areas, and CDHD does not exceed 1 day, while the annual average frequency of CDHSE in Shanxi Province exceeds 4 days, and the annual average longest duration of CDHSE in Shanxi, Chongqing, Hunan, Jiangxi, Jiangsu, Zhejiang, and Shanghai exceeds 1 day and

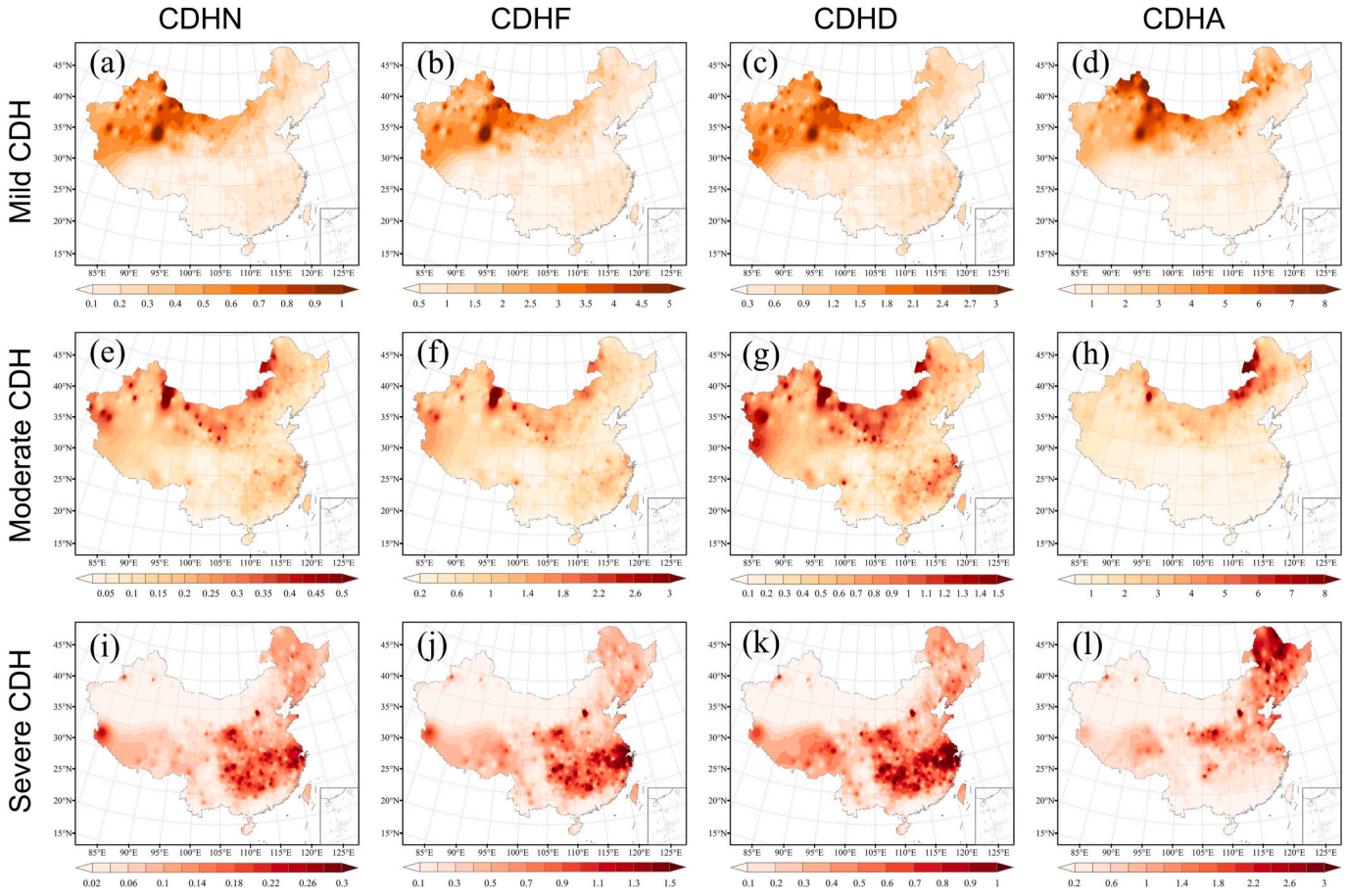

Fig. 3. Spatial patterns of CDH characteristics of different severities across China in the summer (May–September) during 1961–2017. (a-d) CDHN, CDHF, CDHD, CDHA for mild CDH; (e-h) CDHN, CDHF, CDHD, CDHA for moderate CDH; (i-l) CDHN, CDHF, CDHD, CDHA for severe CDH.

reaches >2 days in local areas. Fig. 3 (d, h, l) shows the CDHA distribution of the CDH events. It can be observed that the CDHA of CDHMI and CDHMO has a certain regularity with latitude, with lower peak intensity in the southern region and higher peak intensity in the northern region. On the contrary, CDHSE has a higher peak intensity (CDHA) in the Northeast China, Shanxi and Gansu, and lower peak intensity in the northwest and southern coastal regions.

4.1.2. Temporal evolution of CDH characteristics

This section assesses and analyzes the statistical patterns of fluctuations in the number (CDHN), frequency (CDHF), longest duration (CDHD), and peak value (CDHA) of mild, moderate, and severe CDH events in China from 1961 to 2017. Over the years, we estimated the time series of the station means of each indices of CDH events in China, tested the time series for mutation using the Pettitt test, and determined the change trend using the linear fitting method. Fig. 4 displays the evolution of each characteristic before and after the CDH event mutation, as well as the general growth trend (detailed data results are listed in Table S3). The CDHN, CDHF, CDHD, and CDHA of the three levels all increased significantly during 1961 to 2017, with some variations in the rate of rise, with CDHMI>CDHMO>CDHSE. Each CDH indices was mutated in 1993 or 1996, and the differences before and after the mutation are significant, with all CDH indices after the mutation reaching 2–4 times those before the mutation. Concurrent droughts and heat waves are increasing and will continue to increase, a result that appears to correspond to the increased frequency of dry and hot in the preceding two decades. We also reached an intriguing conclusion. The same indices of CDHMI, CDHMO, and CDHSE stayed practically at the same level prior to the mutation year, but after the mutation year, they showed considerable and regular variability as CDHMI>CDHMO>CDHSE. This indicates that after the period of 1993–1996, heat waves tended to occur more concurrently with mild drought, and the duration of mild CDH events was longer, with a larger heat waves peak.

The temporal evolution patterns of the CDH events vary significantly between sub-regions. Fig. 5(a-g) shows the time series of the CDHN station means for each of the seven sub-regions. Obviously, all CDHNs increased significantly, with the exception of Northwest China (NWC), where the number of CDHSE was nearly zero. Fig. 5(h-j) depicts the CDHN in the seven subregions by year of mutation, as well as the difference in levels before and after mutation. The majority of CDHNs mutated in the 1990s, while mild CDHN in SWC mutated in 1988, severe CDHN in WC mutated in 2005, and all CDHNs in SEC mutated in 2002. Our data revealed that the majority of CDHNs were 2–5 times greater after mutation than before mutation, whereas the severe CDHN of NEC was >6 times higher after mutation. More specifically, the regions with the highest number of CDHMI, CDHMO, and CDHSE before the mutation were NWC, NWC, and EC, respectively, while the regions with the lowest number were SWC, SWC, and NWC. Following the mutation, the regions with the highest number of CDHMI, CDHMO, and CDHSE were NWC, NWC, and NEC, respectively, whereas the regions with the lowest number of CDHMI, CDHMO, and CDHSE were still SWC, SWC, and NWC, respectively. Figs. S4–S6 depicts the time series of CDHF, CDHD, and CDHA in each subregion.

To present the detailed spatial variability of the CDH characteristics evolution, we perform the improved Pettitt test on the CDH characteristics at each station. The abrupt changes and magnitudes of the characteristics are highly consistent in space (Fig. 6). Only the mild CDH characteristics in the northern region show significant step changes (satisfy the $p < p_{FDR}$ criteria), occurring between 1992 and 1998 (dark red). Nonetheless, the potential step change points detected by Pettitt test appear between 1986 and 2010 in a large area (red color scheme), without exception for the moderate and severe CDH characteristics. Unusually, the potential step change points for the severe CDH characteristics in the northwest and southern regions occurred between 1961

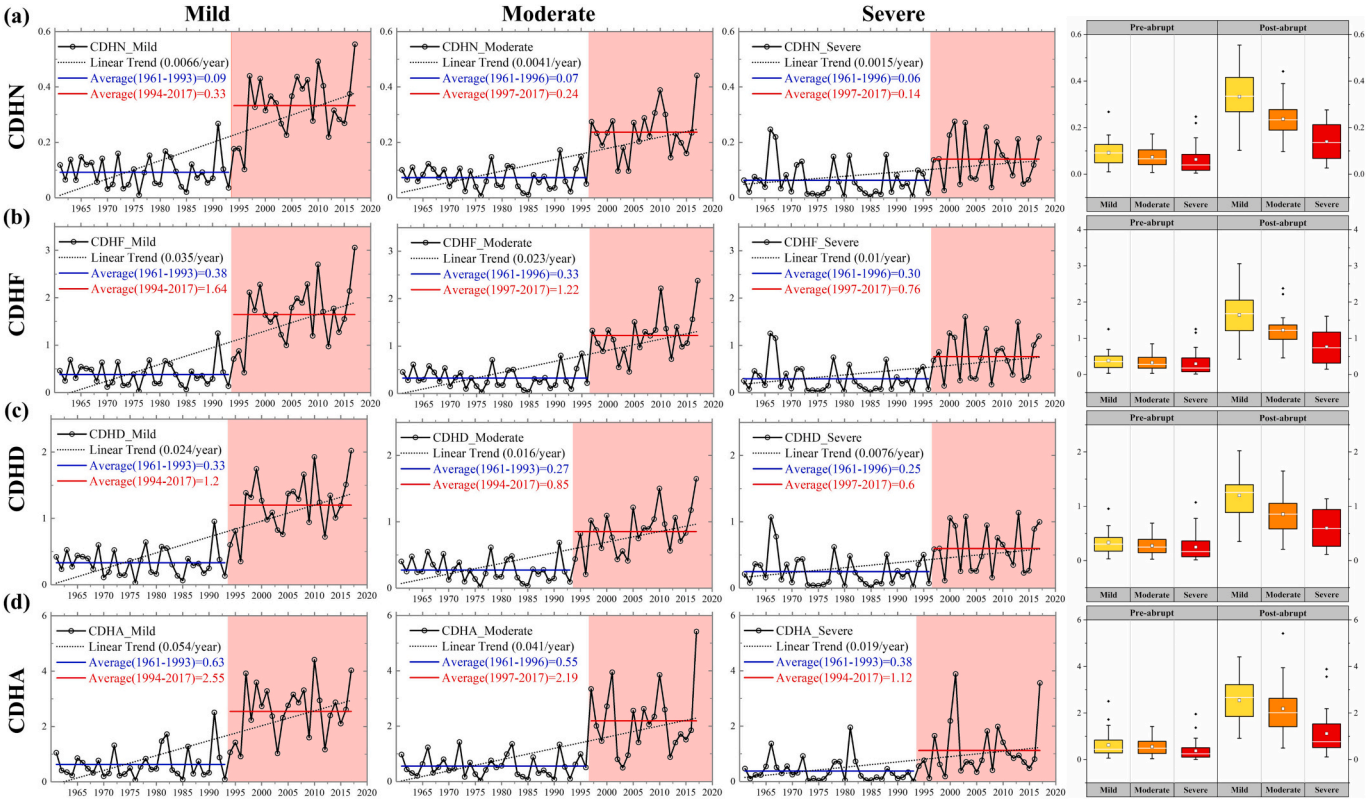

Fig. 4. Characteristics of mild, moderate, and severe CDH events over summers (May to September) averaged over China during 1961–2017. (a) The number of CDH events (CDHN); (b) the total participating days of CDH events (CDHF); (c) the longest duration of CDH events (CDHD); (d) the peak amplitude of heat waves in CDH events (CDHA). The right panel shows the mean value of each characteristic of CDH before and after the abrupt mutation.

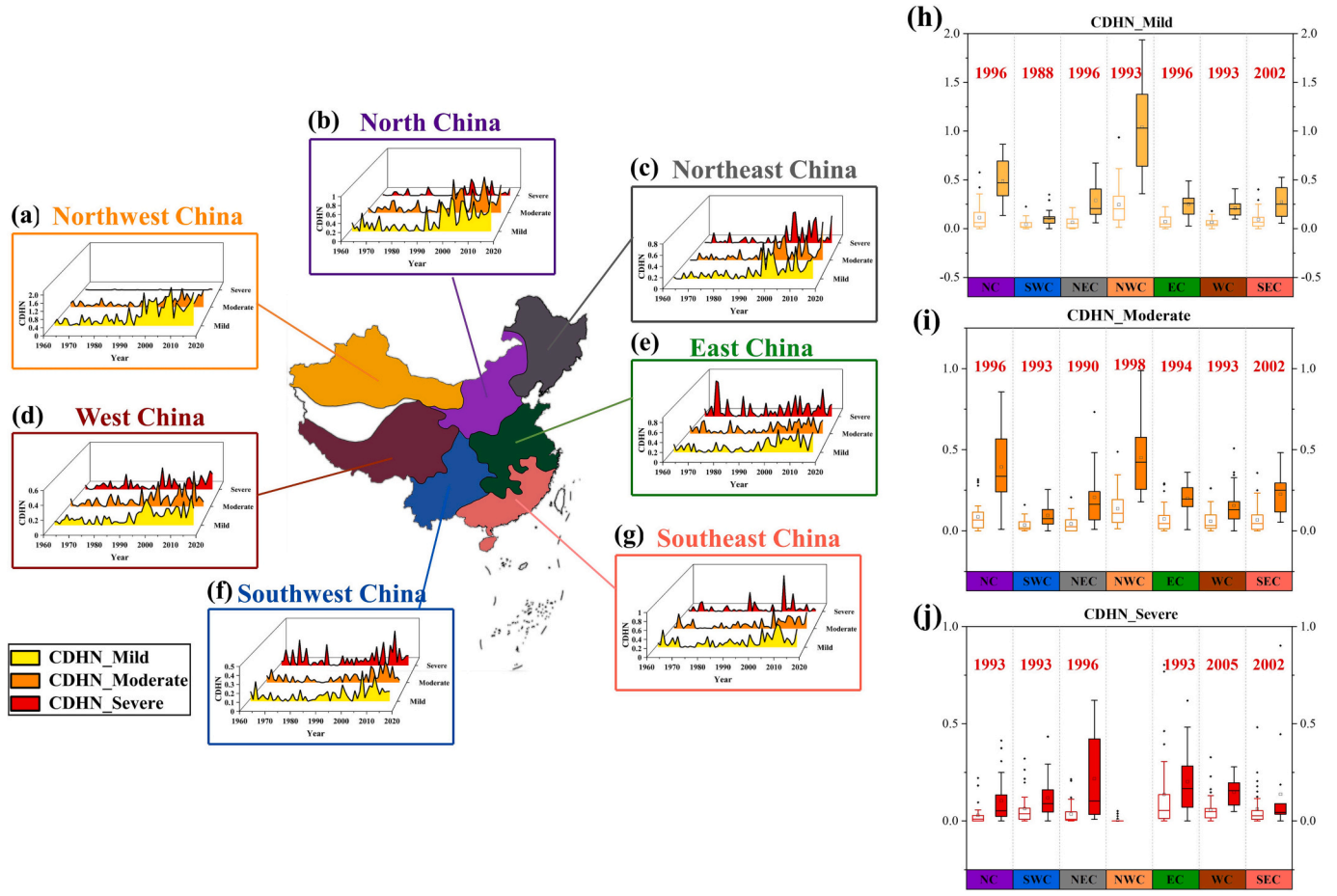

Fig. 5. The evolutions of the number of CDH events in different regions. (a-g) Time series of the number of CDH (CDHN) in each subregion. (h-j) The number of CDH events during the pre-abrupt and post-abrupt periods in different regions. The blank shaded area indicates the regions without meteorological stations.

and 1966 (light blue). This phenomenon is largely explained by the extremely small identifiable sample size of severe CDH events in these regions, with some sites not experiencing severe CDH events during the study period. The change magnitude basically showed a pattern of large for the mild and small for the severe. The change magnitude of mild and moderate CDH characteristics is prominent in the northern and some eastern regions, while the severe CDH characteristics have a more conspicuous change magnitude in the northeastern and central regions. A strong connection is found between this result and the spatial distribution of CDH characteristics. We give the percentage of sites with a range of *p*-values in the bottom left corner of the corresponding spatial map. Multiple tests have a large influence on the results that are statistically significant. Although some areas have small p-values (<0.05 or < 0.1), controlling the FDR yields fewer significant results. Notably, the change magnitude is also larger for sites with red color scheme (1986–2010), where a significant proportion of our results are also in the common range of statistically significant p-values. These results further illustrate that the overall conclusion about the significance of CDH growth and abrupt changes across China and the regional variability is unquestionable.

4.2. Relationship between SST variation and CDHs

The heterogeneous correlations between global SST and CDH characteristics based on leading SVD mode are shown in Fig. 7 with May–September SST as the left field and CDH characteristics as the right field. The heterogeneous correlation of spatial pattern of global SST with CDHN, CDHF, CDHD, and CDHA are remarkably (see Fig. S8 for details). Fig. 7(A-C) shows the spatial patterns of the correlation between global SST and CDHN. The spatial patterns of SST field have heterogeneous correlation coefficients corresponding to mild and moderate CDH events with a wide range of negative values, while those corresponding to severe CDH events have a wide range of positive values, with confidence levels above 95 % in large areas. The spatial patterns of the leading SVD mode with various severity CDH characteristics are both positively and negatively distributed with the corresponding global SST spatial pattern (Fig. 7(a-l)). When the global SST decreases, the characteristics of mild and moderate CDH events in China will be widely reduced or weakened, while when the global SST increases, the characteristics of severe CDH events will be widely increased or strengthened. A positive correlation between global SST and mild, moderate, and severe CDH events is precisely indicated by this outcome. For the CDHMI indices, the confidence level exceeds 95 % in NWC, NC and part of NEC; for the CDHMO indices, the confidence level exceeds 95 % in a few regions in NWC, NC and NEC; while for the CDHSE indices, only very few regions in NEC and east-central China have confidence levels above 95 %. The squared covariance scores for the leading SVD modes (Table 3) are higher than those for the others, suggesting the major association between SST and CDH characteristics. The correlation coefficients of CDHN, CDHF, CDHD, and CDHA indices with global SST for mild CDH events are 0.85, 0.85, 0.86, and 0.80, respectively; 0.90, 0.89, 0.87, and 0.73 for moderate CDH events; and 0.77, 0.73, 0.74, and 0.62 for severe CDH events, respectively. The correlation distributions in Fig. 7(a, b, c) are similar, with positive correlation in the NWC, NC, and partly NEC, and the positive correlation is stronger in the NWC, indicating that the decrease in the number, frequency, and duration of mild CDH events in these

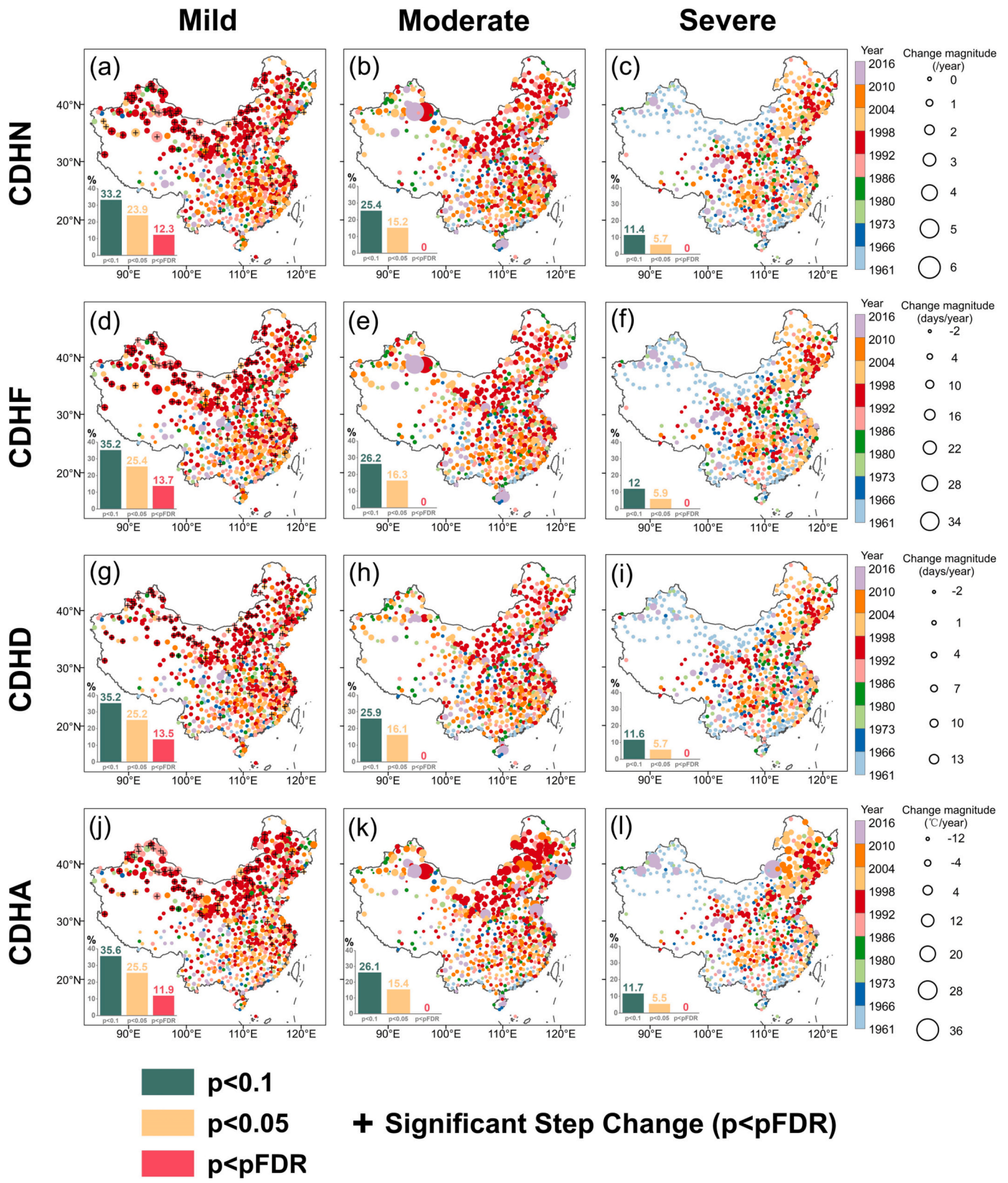

Fig. 6. CDH characteristics potential step change points and change magnitude from 1961 to 2017. The "+" represents satisfying our significant step change criterion ($p < p_{FDR}$), the color indicates the year in which the change point is located, and the site size indicates the magnitude of the change. The bottom left corner of the box shows the proportion of sites with different *p*-value ranges.

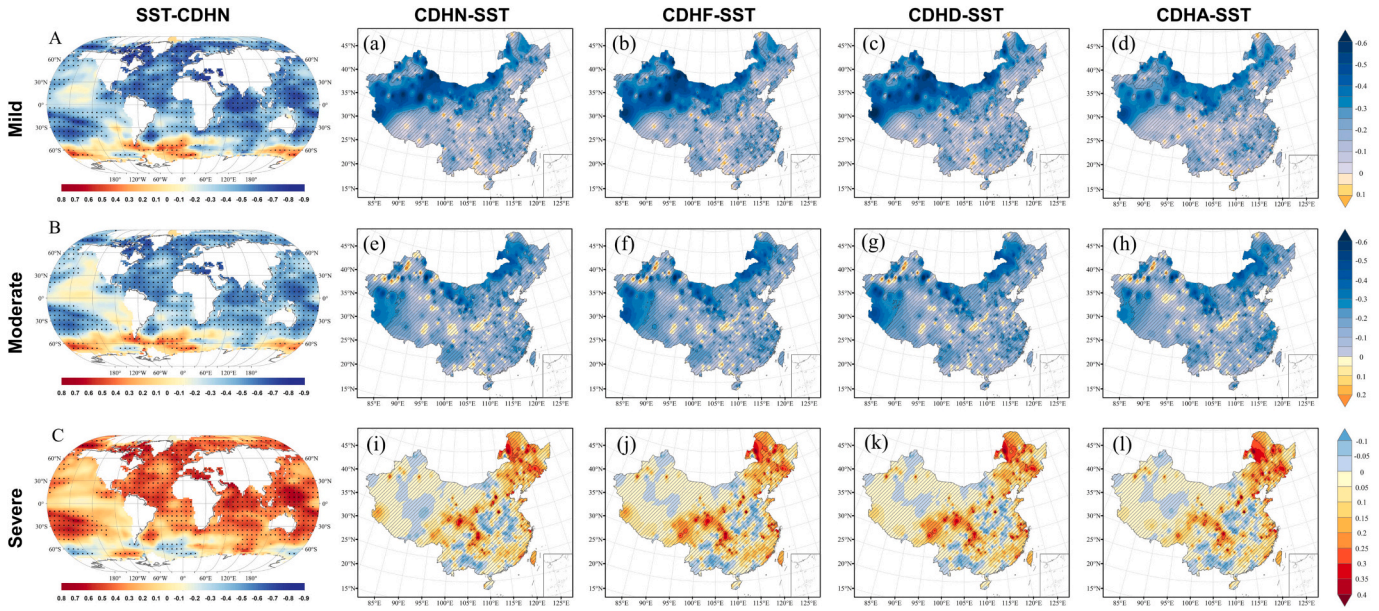

Fig. 7. Heterogeneous correlation of the leading SVD mode between global SST and CDH characteristics. (A-C) Mild, Moderate, Severe SST-CDHN; (a-d) Mild CDHN, CDHF, CDHD, CDHA; (e-h) Moderate CDHN, CDHF, CDHD, CDHA; (i-l) Severe CDHN, CDHF, CDHD, CDHA. The shaded areas with black dot in (A-C) denote that the correlations significant at the 95 % confidence level. The shaded areas except for the hatch area in (a)-(l) denote that the correlations significant at the 95 % confidence level.

Table 3
Squared covariance fraction and heterogeneous correlation of the leading SVD mode between global SST and CDH indices.

	Mild CDH				Moderate CDH				Severe CDH			
	CDHN	CDHF	CDHD	CDHA	CDHN	CDHF	CDHD	CDHA	CDHN	CDHF	CDHD	CDHA
SCF	77 %	78.8 %	73.2 %	74.2 %	72.1 %	75.4 %	66.9 %	70.8 %	45.4 %	52.1 %	49.5 %	61.6 %
Heterogeneous *R*	0.85	0.85	0.86	0.80	0.90	0.89	0.87	0.73	0.77	0.73	0.74	0.62

regions is more likely to be affected by negative SST anomalies. Meanwhile, the amplitude of mild CDH events in these regions exhibits a slight positive correlation with negative SST anomalies (Fig. 7d). Other than the aforementioned regions, the correlation between the mild CDH event indices and SST was nonsignificant. Fig. 7(e, f, g) also show similar correlation distributions as well as positive correlation in various NWC, NC, and NEC. The amplitude of moderate CDH events had a lower positive correlation than the number, frequency, and duration in fewer regions (Fig. 7h). According to Fig. 7(i, j, k, l), the indices of severe CDH events are positively correlated with global SST anomalies in the

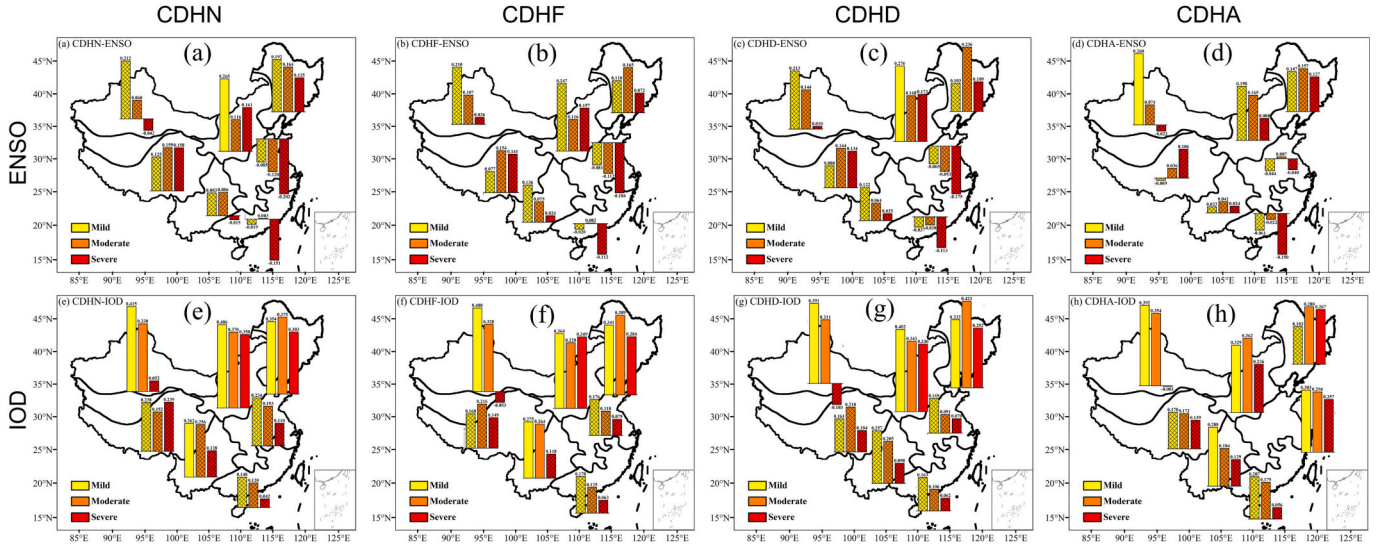

Fig. 8. Pearson correlations between SST modes and CDH characteristics in mild, moderate, and severe events for each subregion. (a) MEI(ENSO)-CDHN; (b) MEI (ENSO)-CDHF; (c) MEI(ENSO)-CDHD; (d) MEI(ENSO)-CDHA; (e) DMI(IOD)-CDHN; (f) DMI(IOD)-CDHF; (g) DMI(IOD)-CDHD; and (h) DMI (IOD)-CDHA. The shaded regions except for the hatch regions in (a-h) denote correlations significant at the 95 % confidence level.

majority of regions, and only a few regions in the Northeast China and individual regions in the east-central region show significant positive correlations. This suggests that the increase of severe CDH events characteristics in the aforementioned regions is driven more likely by positive SST anomalies. Furthermore, the degree of reaction to SST anomalies varied significantly across different levels of CDH episodes. Mild CDH is more vulnerable to SST anomalies than moderate or severe CDH, implying that global SST fluctuations have a stronger impact on mild CDH episodes.

To further investigate the response of CDH events in each sub-region of China to the major SST variations ENSO and IOD, we calculated the Pearson correlation coefficients of the CDH indices of each sub-region with the indices MEI and DMI of ENSO and IOD, respectively, and the results can be used to validate the results of the SVD singular matrix decomposition. Fig. 8(a-d) depict the Pearson correlation coefficients between the year-by-year ENSO index MEI and the CDHN, CDHF, CDHD, and CDHA for each sub-region mean. The correlations between the CDH indices and the MEI (ENSO) in most subregions are insignificant, with only mild CDHN and mild CDHD for NC, mild CDHA for NWC exceeding 95 %, with Pearson correlation coefficients of 0.265, 0.276, and 0.260, respectively. These confidence levels above 95 % are clearly all mild CDH, indicating that mild CDH are more vulnerable to ENSO. In terms of correlation distribution pattern with ENSO, the CDHN, CDHF, and CDHD have a similar regional distribution, while the CDHA is often less correlated in regions other than the NWC. The Pearson correlation coefficients between the IOD year-by-year index DMI and the CDHN, CDHF, CDHD, and CDHA for each sub-region mean are depicted in Fig. 8 (e-h). In comparison to the MEI (ENSO), more sub-regional CDH indices show significant correlation (confidence level >95 %) with the DMI (IOD), with mild and moderate CDH events being more vulnerable to IOD than severe CDH events. All three CDH events in NEC and NC have significant correlations with the DMI index in terms of number, frequency, and duration. All of these subregions, NEC, NC, NWC, SWC, and EC, have certain CDH events that are significantly and positively correlated with DMI(IOD) in terms of CDHA. In terms of correlation distribution pattern with IOD, the CDHN, CDHF, and CDHD have a roughly comparable spatial distribution, however, the response of CDHA to IOD in the EC is greater than the CDHN, CDHF, and CDHD. Overall, the Pearson correlation between CDH events and IOD is greater, indicating that CDH events are more sensitive to IOD than ENSO.

This subsection investigates the extent to which different levels of CDH features respond to anomalous changes in SST using global SST and two major SST variations (ENSO, IOD). The intensity of the warm ENSO event and the positive IOD phase grow as the SST increase, resulting in stronger responses of CDH characteristics. Therefore, we used the composite diagram to examine the differences in CDH changes between the warm (positive) and cold (negative) phases.

4.3. Responses of CDH to lead-simultaneous ENSO and IOD phases

ENSO and IOD at mature periods can have a delayed effect on the climate over China in the following summer. This section focuses on exploring the effect of lead and simultaneous SST modes on CDH, i.e., all years (1961–2017) are divided into the El Niño and La Niña (ENSO) and positive and negative (IOD) phases based on the lead mature (DJF for ENSO and SON for IOD) and simultaneous (May–September) periods of SST modes, respectively. The composite maps of CDH characteristics are obtained by El Niño minus La Niña for ENSO and positive minus negative for IOD in the lead and simultaneous periods, respectively. This approach contributes to our understanding of the differences in the influence of positive and negative phases of SST modes on CDH during two different periods (Wu et al., 2021a).

The differences in the composite analysis of CDH characteristics calculated between the ENSO phases (El Niño minus La Niña) are shown in Fig. 9, where (a-l) are calculated during the following summer of the lead DJF (0) seasons and (m-x) are calculated during the simultaneous summers (1). The lead-simultaneous ENSO has little effect on CDHN in most parts of China (Fig. 9 (a-c) and (m-o)), and the distribution of the effect of the (0) and (1) ENSO phases on CDHN is similar. For mild and moderate CDH, the (0) and (1) ENSO phases cause a decrease in CDHN in the northwest, northeast and east, but the negative anomalies are not significant, and only a few northwest and northern regions have a modest rise; For severe CDH, the (0) and (1) ENSO phases result in a decrease in CDHN in the eastern region, as well as a few northwestern and northeastern regions, and the negative anomalies are also insignificant, except for a significant decrease of >0.3 times in some eastern regions. The CDHF is influenced by the ENSO phase as shown in Fig. 9(d-f) and (p-r). For mild CDH, there is a minor decrease in CDHF affected by the ENSO phases in most of the regions, except for parts of the north, west, and southwest, where there is an increase; For moderate CDH, the (0) and (1) ENSO phases cause a more evident fall in CDHF in the north and certain eastern regions, and a minor but insignificant increase in CDHF in the northwest and west-central regions; For severe CDH, the (0) and (1) ENSO phases lead to a more noticeable decline in CDHF in the eastern region, where the (0) ENSO phases lead to a 1.5 days decrease in some eastern regions, while the amount of change following the impact of severe CDHF in other places is less. The CDHD is also influenced by the ENSO phases (Fig. 9(g-i) and (s-u)), and its distribution resembles that of CDHF. Similarly, the (0) ENSO phases have a significant negative effect on severe CDHD in the eastern region, with a significant reduction of >1 day. Fig. 9(j-l) and (v-x) show the variation of CDHA under the influence of (0) and (1) ENSO phases. The distributions of the CDHA effects of the (0) and (1) ENSO phases are highly similar. For mild CDH, there is a more noticeable increase in CDHA in the northwest, north, and part of the northeast, while there is a more noticeable decline in the west-central and part of the northeast, and most other regions are influenced to a lesser extent; For moderate CDH, there is a greater decline in CDHA in the north and part of the northeast, while there is a little increase in the northwest and lower latitudes of the northeast, with little change in other regions; For severe CDH, except for a noticeable increase or decrease in CDHA in the northeast, most regions have seen relatively little change after being affected by the (0) and (1) ENSO phases. The results in Fig. 9 reveal that the influences of the (0) ENSO phases on the CDH characteristics have some degree of uniformity in distribution, and that these effects are virtually always insignificant. Further, the lead-simultaneous ENSO have more positive impacts on the CDHA and more negative impacts on the CDHN, CDHF, and CDHD.

Fig. 10 shows the differences in composite analysis of CDH characteristics calculated between IOD phases (positive minus negative), where (a-l) are calculated during the following summers of lead SON (0) seasons and (m-x) are calculated during the simultaneous summers (1). For mild CDH, the effects on CDHN, CDHF, CDHD, and CDHA are nearly comparable between the (0) and (1) IOD phases, showing a significant positive effect widely in the northern and some western regions and little effect in rest regions. For moderate CDH, the (0) IOD phases have more significant positive impact on the CDH characteristics in a few northern regions, but the (1) IOD phases have more significant positive effect than the (0) phases in these regions. Particularly, the (1) IOD phases result in relatively significant increase in moderate CDHA in the northeast. For severe CDH, the characteristics are much more weakly affected by the lead-simultaneous IOD phases. The distribution of the effects of the (0) IOD phases on the characteristics of severe CDH is remarkably similar to that of the (1) IOD phases on them. Furthermore, due to the influence of the (0) IOD phases, CDHN, CDHF, CDHD, and CDHA show more significant positive effects in the border areas of Liaoning and Jilin provinces. Overall, the (1) IOD phases have more pronounced effects on CDH characteristics than that in the (0) period, suggesting that the CDH events would increase if the (1) IOD phases occur. From another perspective, mild CDH have a greater response to the lead-simultaneous IOD phases, followed by moderate CDH, and severe CDH has a lower response.

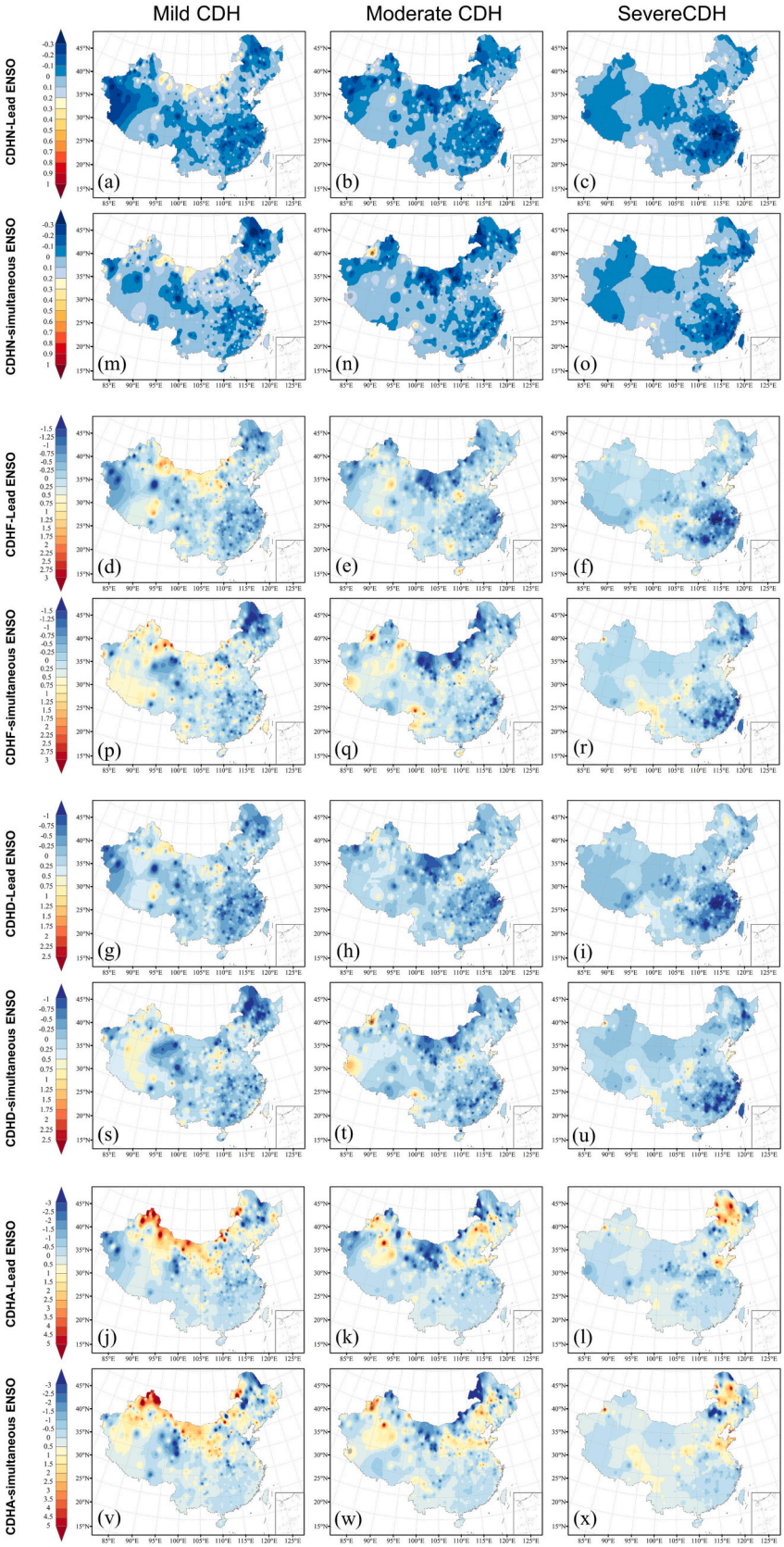

Fig. 9. Composite maps of differences in CDH characteristics calculated during the ENSO (El Niño minus La Niña) phase. (a-l) Lead period; (m-x) Simultaneous period. Hatching denotes statistical significance according to a standard *t*-test at the 95 % confidence level.

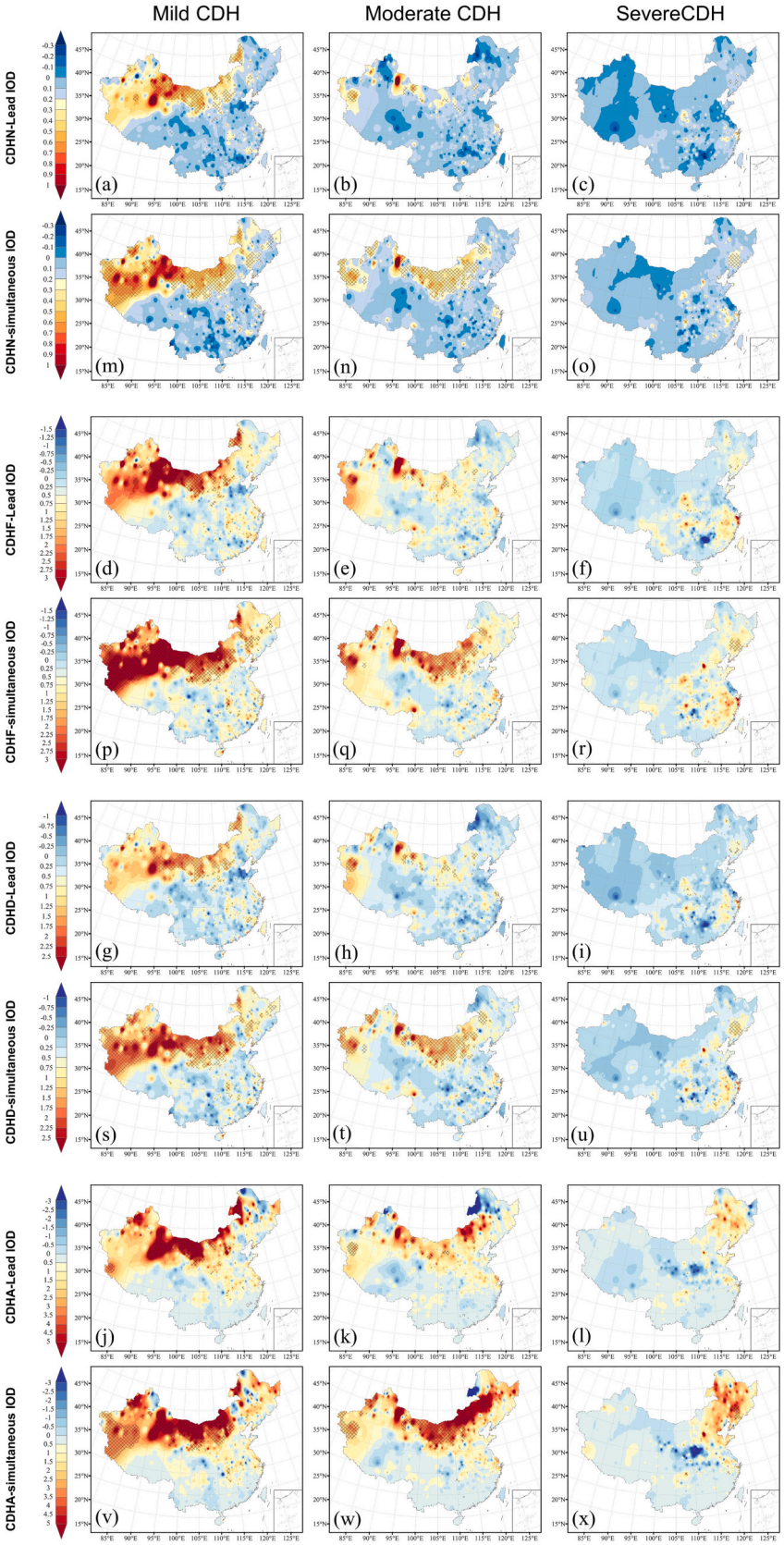

Fig. 10. Composite maps of differences in CDH characteristics calculated during the IOD (positive minus negative) phase. (a-l) Lead period; (m-x) Simultaneous period. Hatching denotes statistical significance according to standard t-test at the 95 % confidence level.

5. Discussion

A widespread abrupt change in various characteristics of the CDH occurred throughout the 1990s, showing that aspects of the CDH event grew rapidly following this period. This discovery is consistent with the findings of other earlier researches (Li et al., 2019; Lu et al., 2018; Wu et al., 2019a, 2019b; Ye et al., 2019). The characteristics of CDH in the northwestern and northern regions are alarmingly high, and relevant studies are available to back up our findings (Xu and Luo, 2019). However, the severe CDH appears to be uncommon in these areas, but is more prevalent in the southeast and northeast. Previous studies demonstrated that the probability of CDH events is highest in southern China, with severe compound events occurring primarily in the region (Li et al., 2021; Wu et al., 2021a, 2021b). The mean summer air temperatures in eastern and southern China are significantly higher than other regions except Xinjiang (Fig. 11.a), with more severe heat waves also more likely to occur in the southern China (Wei et al., 2020). The negative correlation dependence of temperature and soil moisture can affect the severity and regionality of drought-heatwave compound events (Zhang et al., 2022). We calculated the correlation coefficients between monthly air temperature and precipitation, as well as air temperature and surface soil moisture during the summer months (May–September) of 1961–2022. The negative correlation between temperature and precipitation was only observed in southeastern China (Fig. 11.b), accompanied by a strong negative correlation between temperature and soil moisture (Fig. 11.c). Insufficient soil moisture due to lack of precipitation results in reduced evaporative cooling along with enhanced thermal induction and higher surface air temperatures, which accelerates evapotranspiration and further depletes soil moisture (Liu et al., 2020; Miralles et al., 2019). Furthermore, low cloudiness related to lack of precipitation (and consequent soil moisture deficits) tends to reinforce shortwave radiation, leading to higher surface air temperatures (Gentine et al., 2015; Zscheischler and Seneviratne, 2017). These processes combine to result in a strong negative correlation between soil moisture and temperature over large of eastern China (Zhang et al., 2022), which may explain why severe CDH is mainly found in the southeast regions.

The possible physical mechanisms of ENSO and IOD effects on CDH are discussed here. Fig. 12 illustrates the sea level pressure (SLP), 500-hPa geopotential height, and total cloud cover anomalies of ENSO and IOD for the lead and simultaneous phases. During the ENSO lead mature phases, significant positive SLP anomalies are observed across the western Pacific Ocean and southwest China, with no SLP anomalies over most of China (Fig. 12.a). The 500-hPa geopotential height shows significant positive anomalies (Fig. 12.e), implying a drop in pressure, which usually leads to a decline in temperature and more precipitation due to cooling of the updrafts. Increased cloud cover reduces solar radiation to cool temperatures and facilitates precipitation formation, especially in northwest and southeast China (Fig. 12.i), resulting in reduced CDH. During the ENSO simultaneous phases, there are no cloud cover anomalies over most of China, except for a significant reduction in northern China (Fig. 12.j). Significant positive SLP and 500-hPa geopotential height anomalies move westward to envelop most of China (Fig. 12.b and f), leading to a decrease in temperature and possibly triggering convective activity at the high-pressure margin to increase precipitation and ultimately resulting in less CDH.

During the lead IOD phases, the positive SLP anomalies appeared near the equator and in the north of China (Fig. 12.c), and the positive 500-hPa geopotential height anomalies dominated the area around China, especially in the northwestern part (Fig. 12.g), which may reverse the effect of increased cloud cover (Fig. 12.k), contributing to warmer temperatures and less precipitation in northern China. In contrast, during the IOD simultaneous phases, the center of negative anomalies occurs over the North Pacific Ocean, weak negative SLP anomalies occupy most of China (Fig. 12.d), tropical cyclones with accompanying high temperatures may occur, and the low-pressure

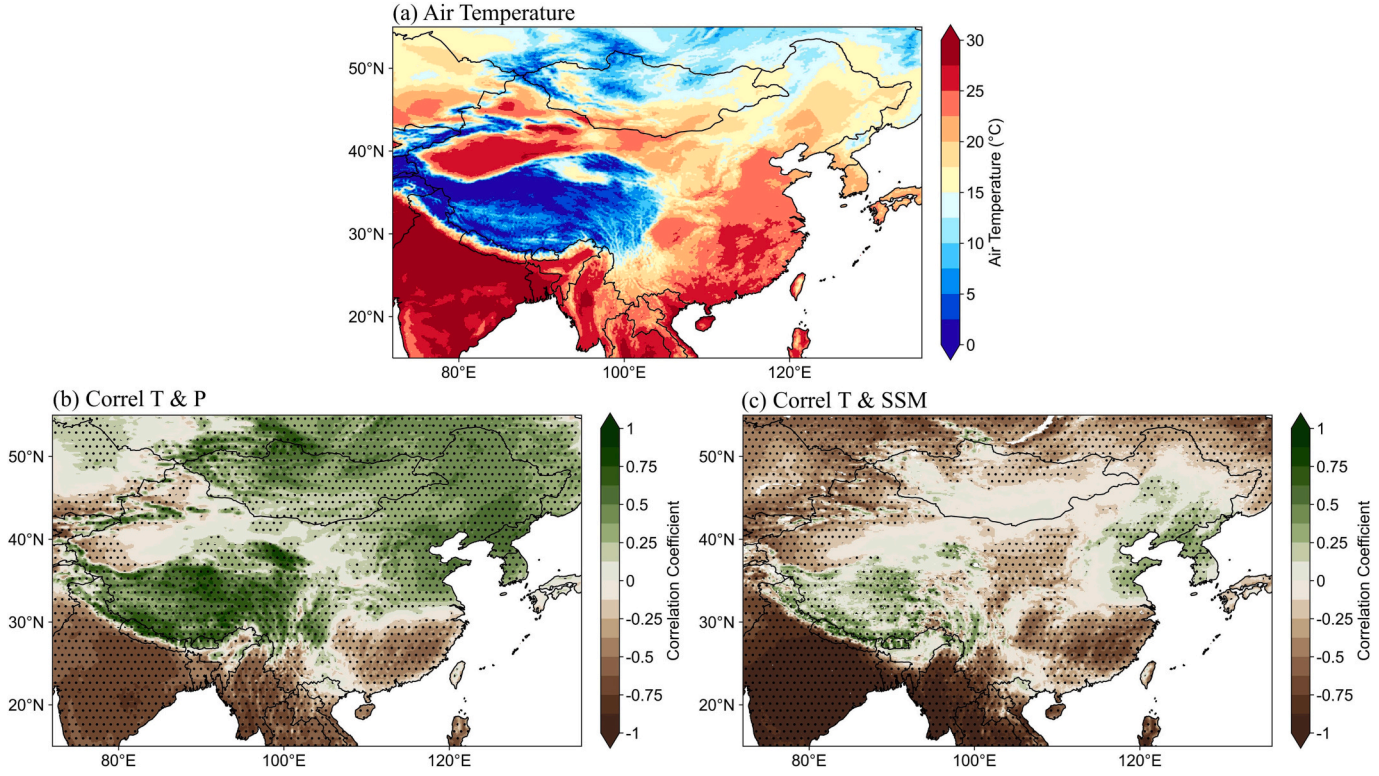

Fig. 11. (a) The spatial distribution of the mean temperature in summertime (May–September) from 1961 to 2022; The spatial distribution of correlation coefficients between monthly air temperature and precipitation (b) and between air temperature and surface soil moisture (c) in summer (May–September) from 1961 to 2022. The shaded areas with black dots in (b) and (c) indicate the correlations significant at the 95 % confidence level.

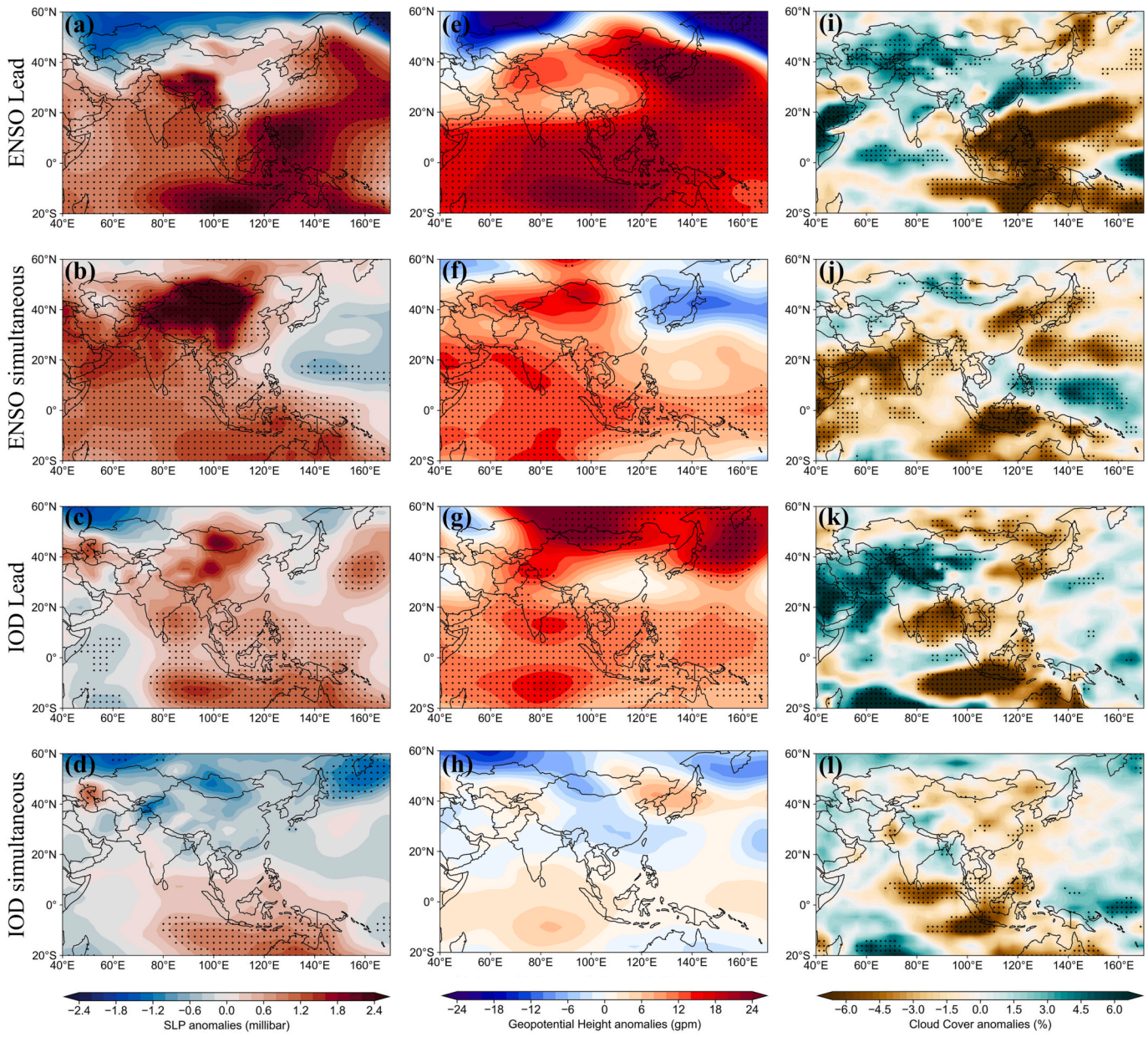

Fig. 12. The differences between the composite maps of the sea-level pressure (millibar) (a-d), 500-hPa geopotential height (gpm) (e-h) and total cloud cover (%) (i-l) anomalies for the ENSO (El Niño-La Niña) and IOD (positive-negative) during the anomalous seasons. The shaded areas with black dots indicate the anomalies significant at 95 % confidence level on a standard t-test.

system may impede the development of convection thus decreasing precipitation, resulting in higher CDH in northern China. Moreover, most of China was occupied by weak 500-hPa geopotential height negative anomalies (Fig. 12.h), which led to a rise in air pressure and compression of atmospheric subsidence, resulting in higher temperatures and evaporation of water vapor, which reduced the cloud cover and hence less probability of precipitation formation (Fig. 12.l), and ultimately increasing the CDH events.

Other large-scale forcings such as the PDO, AMO, and NAO (Wu et al., 2021a, 2021b), should be explored beyond the focus of our study. The PDO and NAO may affect the occurrence of CDH events independently or in conjunction with ENSO and IOD, which may enhance or diminish their effects (Chang et al., 2006; Saji and Yamagata, 2003). Pearson correlation coefficients were calculated for the annual average index of NAO, AMO, and PDO with each CDH characteristic from 1961 to 2017. Almost all CDH characteristics showed significant positive correlations with AMO and less correlations with NAO and PDO (Fig. 13. a-d). The correlation coefficients of CDH characteristics between NAO (in three regions), NC, NEC, and SEC, were somewhat prominent, although not all were significantly correlated. Perhaps NAO has contributed to the variations of CDH within certain regions of China. Throughout, the results suggest that AMO is more closely associated with CDH growth across China, which is intriguing. Since AMO has a 60–80 years cycle, the Composite Analysis is obviously not applicable here. The AMO trends during the simultaneous CDH study period exhibit a positive phase change during 1961–2017 (Fig. 13.e). Note that the AMO positive phase change is positioned close to the abrupt change in CDH characteristics (in terms of the national average CDHN), suggesting that the abrupt increase in CDH characteristics can be assumed to come from a significantly enhanced coefficient of AMO. We are convinced that this is a topic worthy of deeper research and would be another major research (Wei et al., 2023), although the research framework of this paper is not enough to explore in depth the complex associations of other large-scale SST modes including AMO with summer CDHs across China.

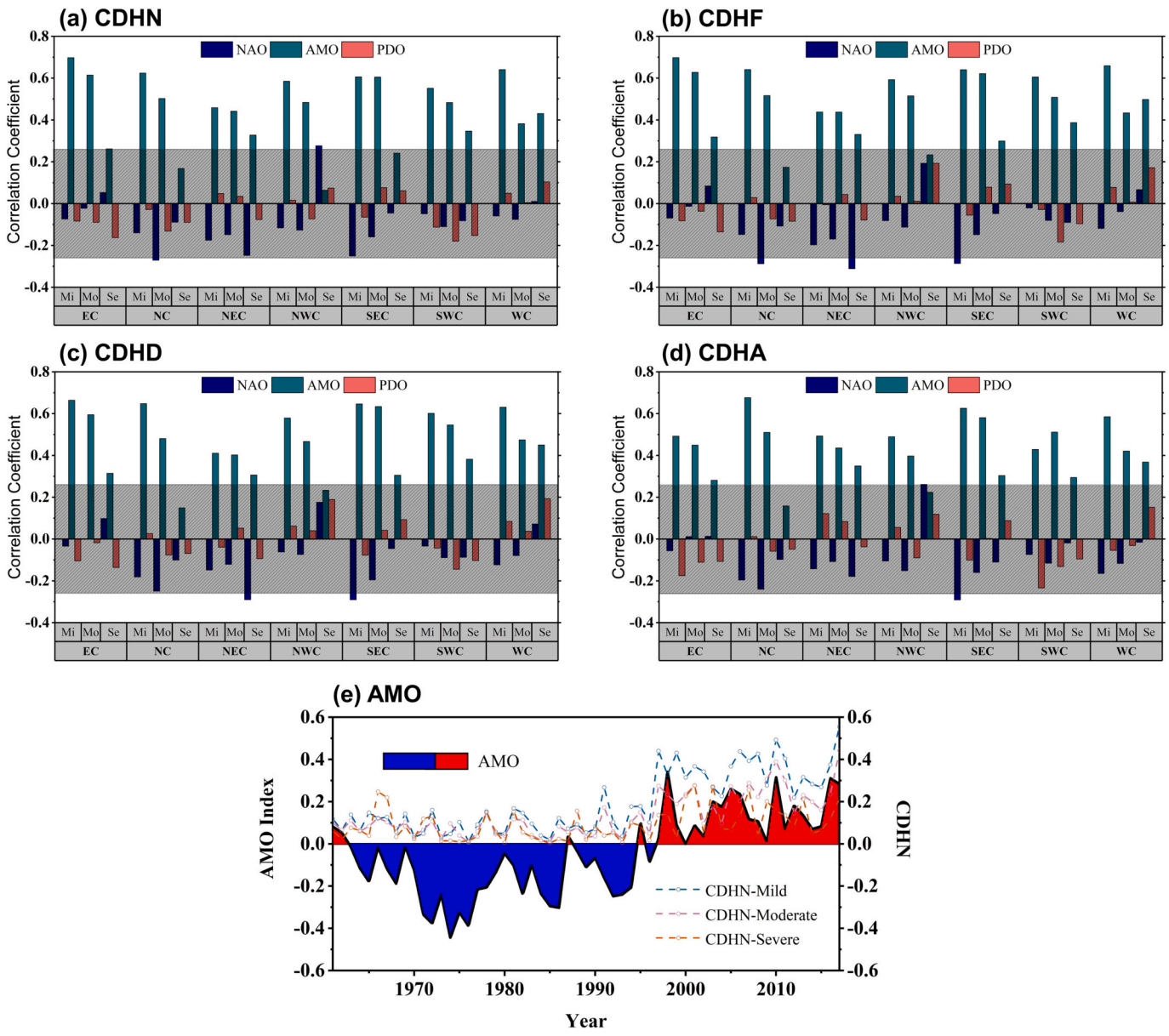

Fig. 13. (a-d) Pearson correlation coefficients for the mean annual index of NAO, AMO, and PDO with each CDH characteristic from 1961 to 2017; (e) Phase change of AMO and average CDHN trend in China during 1961–2017. The gray shading in (a-d) indicates the threshold range of correlation coefficients for which the correlation is not significant ($p > 0.05$) according to t-test.

Although the findings we report here are based on observational data and available analytical methods, there still remains limitations that should be addressed in further studies. The characterizations of CDH events, for example, is dependent on the indicators used to identify heat waves and droughts. The identification of heat waves will differ if different high temperature heat waves indices are used, and the same is true for drought. When different combinations of drought and heat waves indices are used, the discrepancies in identifying compound drought and heat waves events may be more significant. Moreover, numerous studies on the assessment and attribution of compound drought and heat waves are defining such events as concurrent drought and heat waves, including the present study. Note that with some of the shared drivers of drought and heat waves, heat waves often appear more quickly, whereas drought displays a lag. As a result, more comprehensive definitions of CDH events must be examined further, and future research will focus on a more comprehensive and time-scale uniform compound drought and heat waves index. In addition, this research work only uses data from ground-based weather stations, which may be insufficient in some areas, and interpolation may result in huge uncertainties. For example, in the Qinghai-Tibet Plateau region, there are only a very few stations over a large area, which will inevitably create large errors and uncertainties in the CDH assessment for this region. The relative threshold definition of heat waves used in this work offers apparent advantages for investigating compound event changes in the Qinghai-Tibet Plateau, where the mean temperature is lower. In addition, the variability of CDH event characteristics is often associated with seasonal precipitation and evapotranspiration quantity and variability, and anthropogenic warming (Konapala et al., 2020; Schwingshackl et al., 2017; Zampieri et al., 2017). Therefore, a more comprehensive integration of the relative contributions of these influences could contribute to our understanding of the evolution of CDH.

In this study, a special effort is made to provide a more refined identification of CDH than previous studies, which is necessary because of the large regional spatial variability in China. Compound drought and heat waves events in some regions are more importantly influenced by SST modes that cannot be ignored. Therefore, we tried to investigate the

anomalous variability of CDH characteristics in China by finding a suitable combination of indicators to relate them to the variability of SST modes and to find some meaningful conclusions, thus highlighting the significance of this study. This study reports many changes in the CDH characteristics in China, complementing some parts that were not considered in previous studies and improving a more comprehensive understanding of them. The findings of this study contribute to relevant prediction efforts and can improve disaster prevention and mitigation measures in China's sensitive regions.

6. Conclusions

In this study, the CDH events are accurately identified by using a new framework combining SPEI and EHF, and multifaceted spatial-temporal variations of mild, moderate, and severe CDH events are evaluated. SVD and Pearson correlations are used to explore the correlations between SST variations and compound events, and further composite methods are used to assess the effects of SST modes on CDHN, CDHF, CDHD, and CDHA to reveal the contribution of SST modes to their variations.

Over the past 60 years, the CDH characteristics in China exhibited an intensifying trend with a consistent abrupt increase. The national average after 1993–1996 all reached 2 to 4 times of those in the pre-abrupt period. Our results show that the dry heat trend is unprecedented. The number, frequency, duration and intensity of regional CDH events were heterogeneous and showed a consistent growth trend. Mild and moderate CDH events occurred mostly in the northwestern and northern regions of China, while severe CDH was mainly found in the central and eastern regions. A significant positive correlation was found between mild and moderate CDH characteristics and SST in the northwestern and northern regions, indicating a close association between CDH and SST changes. Pearson correlation experiments also showed stronger correlation between the compound drought and heat waves features and IOD in each sub-region compared with ENSO. Mild and moderate CDH events were more susceptible to SST modes than severe CDH. IOD dominates the exacerbation of mild and moderate CDH events compared to ENSO. Regionally, the northwest and north experienced longer, more frequent and severe CDH events during the positive IOD phase.

CRediT authorship contribution statement

Xiaolong Pan: Data curation, Formal analysis, Methodology, Visualization, Writing - original draft. **Weiguang Wang:** Conceptualization, Funding acquisition, Supervision. **Quanxi Shao:** Investigation. **Jia Wei:** Data curation, Methodology, Visualization. **Hongbin Li:** Visualization. **Fengyan Zhang:** Data curation, Methodology. **Mingzhu Cao:** Data curation. **Liyan Yang:** Visualization.

Declaration of competing interest

The authors declare that they have no known competing financial interests or personal relationships that could have appeared to influence the work reported in this paper.

Data availability

No data was used for the research described in the article.

Acknowledgments

This work is co-funded by the National Natural Science Foundation of China (Key Program; U2240218), the National Natural Science Foundation of China (51979071). Thanks to Doug Richardson (Climate Science Centre, CSIRO Oceans & Atmosphere, Hobart, Tasmania, Australia) for his help in the application of the new Pettitt test. We thank the three anonymous reviewers for their detailed and constructive comments that contributed to improving the quality of the paper.

Appendix A. Supplementary data

Supplementary data to this article can be found online at https://doi.org/10.1016/j.scitotenv.2023.167934.

References

Alizadeh, M.R., Adamowski, J., Nikoo, M.R., AghaKouchak, A., Dennison, P., Sadegh, M., 2020. A century of observations reveals increasing likelihood of continental-scale compound dry-hot extremes. Sci. Adv. 6 (39), 11. Article eaaz4571. https://doi.org/10.1126/sciadv.aaz4571.

Allen, C.D., Macalady, A.K., Chenchouni, H., Bachelet, D., McDowell, N., Vennetier, M., Kitzberger, T., Rigling, A., Breshears, D.D., Hogg, E.H., Gonzalez, P., Fensham, R., Zhang, Z., Castro, J., Demidova, N., Lim, J.H., Allard, G., Running, S.W., Semerci, A., Cobb, N., 2010. A global overview of drought and heat-induced tree mortality reveals emerging climate change risks for forests. For. Ecol. Manag. 259 (4), 660–684. https://doi.org/10.1016/j.foreco.2009.09.001.

Bai, L., Ding, G.Q., Gu, S.H., Bi, P., Su, B.D., Qin, D.H., Xu, G.Z., Liu, Q.Y., 2014. The effects of summer temperature and heat waves on heat-related illness in a coastal city of China, 2011-2013. Environ. Res. 132, 212–219. https://doi.org/10.1016/j.envres.2014.04.002.

Bandyopadhyay, S., Kanji, S., Wang, L.M., 2012. The impact of rainfall and temperature variation on diarrheal prevalence in sub-Saharan Africa. Appl. Geogr. 33 (1), 63–72. https://doi.org/10.1016/j.apgeog.2011.07.017.

Barlow, M., Nigam, S., Berbery, E.H., 2001. ENSO, Pacific decadal variability, and US summertime precipitation, drought, and stream flow. J. Clim. 14 (9), 2105–2128. https://doi.org/10.1175/1520-0442(2001)014<2105:Epdvau>2.0.Co;2.

Barriopedro, D., Garcia-Herrera, R., Lupo, A.R., Hernandez, E., 2006. A climatology of northern hemisphere blocking. J. Clim. 19 (6), 1042–1063. https://doi.org/10.1175/jcli3678.1.

Barriopedro, D., Fischer, E.M., Luterbacher, J., Trigo, R., Garcia-Herrera, R., 2011. The hot summer of 2010: redrawing the temperature record map of Europe. Science 332 (6026), 220–224. https://doi.org/10.1126/science.1201224.

Benjamini, Y., Hochberg, Y., 1995. Controlling the false discovery rate: a practical and powerful approach to multiple testing. J. R. Stat. Soc. Ser. B Methodol. 57, 289–300 (Publisher: John Wiley & Sons, Ltd.).

Bouma, M.J., Kovats, R.S., Goubet, S.A., Cox, J.S.H., Haines, A., 1997. Global assessment of El Nino's disaster burden. Lancet 350 (9089), 1435–1438. https://doi.org/10.1016/s0140-6736(97)04509-1.

Bretherton, C.S., Smith, C., Wallace, J.M., 1992. An intercomparison of methods for finding coupled patterns in climate data, 5 (6), 541–560.

Chang, P., Yamagata, T., Schopf, P., Behera, S.K., Carton, J., Kessler, W.S., Meyers, G., Qu, T., Schott, F., Shetye, S., Xie, S.P., 2006. Climate fluctuations of tropical coupled systems - the role of ocean dynamics. J. Clim. 19 (20), 5122–5174. https://doi.org/10.1175/jcli3903.1.

Chen, H.P., Sun, J.Q., 2015. Changes in drought characteristics over China using the standardized precipitation evapotranspiration index. J. Clim. 28 (13), 5430–5447. https://doi.org/10.1175/jcli-d-14-00707.1.

Cheng, K., He, K.X., Fu, Q., Tagawa, K., Guo, X.X., 2022. Assessing the coordination of regional water and soil resources and ecological-environment system based on speed characteristics. J. Clean. Prod. 339 (9), 130718 https://doi.org/10.1016/j.jclepro.2022.130718.

Chiang, F., Mazdiyasni, O., AghaKouchak, A., 2018. Amplified warming of droughts in southern United States in observations and model simulations. Sci. Adv. 4 (8), 6 (Article eaat2380). https://doi.org/10.1126/sciadv.aat2380.

Coumou, D., Rahmstorf, S., 2012. A decade of weather extremes. Nat. Clim. Chang. 2 (7), 491–496. https://doi.org/10.1038/nclimate1452.

Dai, A.G., Zhao, T.B., 2017. Uncertainties in historical changes and future projections of drought. Part I: estimates of historical drought changes. Clim. Chang. 144 (3), 519–533. https://doi.org/10.1007/s10584-016-1705-2.

De Adana, F.J.S., Colucci, S.J., 2005. Southern hemisphere blocking onsets associated with upper-tropospheric divergence anomalies. J. Atmos. Sci. 62 (5), 1614–1625 (://WOS:000229335800021).

Ding, T., Qian, W.H., 2011. Geographical patterns and temporal variations of regional dry and wet heatwave events in China during 1960-2008. Adv. Atmos. Sci. 28 (2), 322–337. https://doi.org/10.1007/s00376-010-9236-7.

Dong, L., Mitra, C., Greer, S., Burt, E., 2018. The dynamical linkage of atmospheric blocking to drought, heatwave and urban heat island in southeastern US: a multi-scale case study. Atmosphere 9 (1), 18 (Article 33). https://doi.org/10.3390/atmos9010033.

Duan, R.X., Huang, G.H., Li, Y.P., Zhou, X., Ren, J.Y., Tian, C.Y., 2021. Stepwise clustering future meteorological drought projection and multi-level factorial analysis under climate change: a case study of the Pearl River Basin, China. Environ. Res. 196 (15), 110368 https://doi.org/10.1016/j.envres.2020.110368.

Feng, P.Y., Wang, B., Liu, D.L., Yu, Q., 2019. Machine learning-based integration of remotely-sensed drought factors can improve the estimation of agricultural drought in south-eastern Australia. Agric. Syst. 173, 303–316. https://doi.org/10.1016/j.agsy.2019.03.015.

Feng, S.F., Hao, Z.C., Wu, X.Y., Zhang, X., Hao, F.H., 2021. A multi-index evaluation of changes in compound dry and hot events of global maize areas. J. Hydrol. 602 (9), 126728 https://doi.org/10.1016/j.jhydrol.2021.126728.

Fink, A.H., Brücher, T., Krüger, A., Leckebusch, G.C., Pinto, J.G., Ulbrich, U., 2004. The 2003 European summer heatwaves and drought -synoptic diagnosis and impacts: European heatwave - impacts. Weather 59, 209–216. https://doi.org/10.1256/wea.73.04.

Fischer, E.M., Seneviratne, S.I., Luthi, D., Schar, C., 2007. Contribution of land-atmosphere coupling to recent European summer heat waves. Geophys. Res. Lett. 34 (6), 6 (Article L06707). https://doi.org/10.1029/2006gl029068.

Gentine, P., Meier, A., Malyshev, S., Lawrence, D.M., Hagemann, S., Chéruy, F., Ducharne, A., van den Hurk, B., Seneviratne, S.I., Findell, K., Lintner, B.R., Berg, A., 2015. Interannual coupling between summertime surface temperature and precipitation over land: processes and implications for climate change*. J. Clim. 28 (3), 1308–1328. https://doi.org/10.1175/jcli-d-14-00324.1.

Grumm, R.H., 2011. The central European and Russian heat event of July-August 2010 [article]. Bull. Am. Meteorol. Soc. 92 (10), 1285–1296. https://doi.org/10.1175/2011bams3174.1.

Hao, Z.C., Hao, F.H., Singh, V.P., Zhang, X., 2018a. Changes in the severity of compound drought and hot extremes over global land areas. Environ. Res. Lett. 13 (12), 8 (Article 124022). https://doi.org/10.1088/1748-9326/aaee96.

Hao, Z.C., Hao, F.H., Singh, V.P., Zhang, X., 2018b. Quantifying the relationship between compound dry and hot events and El Nino-southern oscillation (ENSO) at the global scale. J. Hydrol. 567, 332–338. https://doi.org/10.1016/j.jhydrol.2018.10.022.

Hauser, M., Orth, R., Seneviratne, S.I., 2016. Role of soil moisture versus recent climate change for the 2010 heat wave in western Russia. Geophys. Res. Lett. 43 (6), 2819–2826. https://doi.org/10.1002/2016gl068036.

He, Y., Fang, J.Y., Xu, W., Shi, P.J., 2022. Substantial increase of compound droughts and heatwaves in wheat growing seasons worldwide. Int. J. Climatol. 42 (10), 5038–5054. https://doi.org/10.1002/joc.7518.

Hong, C.-C., Li, T., Ho, Lin, Kug, J.-S., 2008. Asymmetry of the Indian Ocean dipole. Part I: observational analysis. J. Clim. 21 (18), 4834–4848. https://doi.org/10.1175/2008jcli2222.1.

Hong, C.-C., Li, T., LinHo, & Chen, Y.-C., 2010. Asymmetry of the Indian Ocean Basinwide SST anomalies: roles of ENSO and IOD. J. Clim. 23 (13), 3563–3576. https://doi.org/10.1175/2010jcli3320.1.

Hua, W., Dai, A., Qin, M., Hu, Y., Cui, Y., 2023. *How Unexpected Was the 2022 Summertime Heat Extremes in the Middle Reaches of the Yangtze River?* Geophys. Res. Lett. 50, e2023GL104269 https://doi.org/10.1029/2023GL104269.

Huang, B.Y., Thorne, P.W., Banzon, V.F., Boyer, T., Chepurin, G., Lawrimore, J.H., Menne, M.J., Smith, T.M., Vose, R.S., Zhang, H.M., 2017. Extended reconstructed sea surface temperature, version 5 (ERSSTv5): upgrades, validations, and intercomparisons. J. Clim. 30 (20), 8179–8205. https://doi.org/10.1175/jcli-d-16-0836.1.

Kang, S., Eltahir, E.A.B., 2018. North China plain threatened by deadly heatwaves due to climate change and irrigation. Nat. Commun. 9 (9), 2894 https://doi.org/10.1038/s41467-018-05252-y.

Kogan, F.N., 2000. Satellite-observed sensitivity of world land ecosystems to El Nino/La Nina. Remote Sens. Environ. 74 (3), 445–462. https://doi.org/10.1016/s0034-4257(00)00137-1.

Konapala, G., Mishra, A.K., Wada, Y., Mann, M.E., 2020. Climate change will affect global water availability through compounding changes in seasonal precipitation and evaporation. Nat. Commun. 11 (1), 10. https://doi.org/10.1038/s41467-020-16757-w.

Kong, Q.Q., Guerreiro, S.B., Blenkinsop, S., Li, X.F., Fowler, H.J., 2020. Increases in summertime concurrent drought and heatwave in eastern China. Weather Clim. Extremes 28 (8), 100242. https://doi.org/10.1016/j.wace.2019.100242.

Kunsch, H.R., 1989. The jackknife and the bootstrap for general stationary observations. Ann. Stat. 17 (3), 1217–1241. https://doi.org/10.1214/aos/1176347265 ((ISSN: 0090-5364, 2168-8966). Publisher: Institute of Mathematical Statistics).

Lahiri, S.N., 2003. Bootstrap methods. In: Lahiri, S.N. (Ed.), Resampling Methods for Dependent Data, Springer Series in Statistics. Springer, New York, NY, pp. 17–43. https://doi.org/10.1007/978-1-4757-3803-2_2. ISBN: 978-1-4757-3803-2.

Lee, H., 2015. General rainfall patterns in Indonesia and the potential impacts of local seas on rainfall intensity. Water 7, 1751–1768. https://doi.org/10.3390/w7041751.

Leonard, M., Westra, S., Phatak, A., Lambert, M., van den Hurk, B., McInnes, K., Risbey, J., Schuster, S., Jakob, D., Stafford-Smith, M., 2014. A compound event framework for understanding extreme impacts. Wiley Interdiscip. Rev. Clim. Chang. 5 (1), 113–128. https://doi.org/10.1002/wcc.252.

Li, H.X., He, S.P., Gao, Y.Q., Chen, H.P., Wang, H.J., 2020. North Atlantic modulation of interdecadal variations in hot drought events over northeastern China. J. Clim. 33 (10), 4315–4332. https://doi.org/10.1175/jcli-d-19-0440.1.

Li, J., Wang, Z.L., Wu, X.S., Zscheischler, J., Guo, S.L., Chen, X.H., 2021. A standardized index for assessing sub-monthly compound dry and hot conditions with application in China. Hydrol. Earth Syst. Sci. 25 (3), 1587–1601. https://doi.org/10.5194/hess-25-1587-2021.

Li, X., You, Q.L., Ren, G.Y., Wang, S.Y., Zhang, Y.Q., Yang, J.L., Zheng, G.F., 2019. Concurrent droughts and hot extremes in northwest China from 1961 to 2017. Int. J. Climatol. 39 (4), 2186–2196. https://doi.org/10.1002/joc.5944.

Lin, W., Wen, C., Wen, Z., Gang, H., 2015. Drought in Southwest China: a review. Atmos. Ocean. Sci. Lett. 8, 339–344. https://doi.org/10.3878/AOSL20150043.

Liu, Q.Y., Feng, M., Wang, D.X., Wijffels, S., 2015. Interannual variability of the Indonesian throughflow transport: a revisit based on 30 year expendable bathythermograph data. J. Geophys. Res. Oceans 120 (12), 8270–8282. https://doi.org/10.1002/2015jc011351.

Liu, X., He, B., Guo, L., Huang, L., Chen, D., 2020. Similarities and differences in the mechanisms causing the European summer heatwaves in 2003, 2010, and 2018. Earth's Future 8 (4). https://doi.org/10.1029/2019ef001386.

Lu, Y., Hu, H.C., Li, C., Tian, F.Q., 2018. Increasing compound events of extreme hot and dry days during growing seasons of wheat and maize in China. Sci. Rep. 8 (8), 16700 https://doi.org/10.1038/s41598-018-34215-y.

Ma, F., Yuan, X., 2023. When will the unprecedented 2022 summer heat waves in Yangtze River basin become normal in a warming climate? Geophys. Res. Lett. 50, e2022GL101946 https://doi.org/10.1029/2022GL101946.

Manning, C., Widmann, M., Bevacqua, E., Van Loon, A.F., Maraun, D., Vrac, M., 2018. Soil moisture drought in Europe: a compound event of precipitation and potential evapotranspiration on multiple time scales. J. Hydrometeorol. 19 (8), 1255–1271. https://doi.org/10.1175/jhm-d-18-0017.1.

Mazdiyasni, O., AghaKouchak, A., 2015. Substantial increase in concurrent droughts and heatwaves in the United States. Proc. Natl. Acad. Sci. U. S. A. 112 (37), 11484–11489. https://doi.org/10.1073/pnas.1422945112.

Miralles, D.G., Gentine, P., Seneviratne, S.I., Teuling, A.J., 2019. Land-atmospheric feedbacks during droughts and heatwaves: state of the science and current challenges. Ann. N. Y. Acad. Sci. 1436 (1), 19–35. https://doi.org/10.1111/nyas.13912.

Mishra, V., Thirumalai, K., Singh, D., Aadhar, S., 2020. Future exacerbation of hot and dry summer monsoon extremes in India. Npj Clim. Atmos. Sci. 3 (1), 9 (Article 10). https://doi.org/10.1038/s41612-020-0113-5.

Mukherjee, S., Ashfaq, M., Mishra, A.K., 2020. Compound drought and heatwaves at a global scale: the role of natural climate variability-associated synoptic patterns and land-surface energy budget anomalies. J. Geophys. Res.-Atmos. 125 (11), 19 (Article e2019JD031943). https://doi.org/10.1029/2019jd031943.

Murari, K.K., Sahana, A.S., Daly, E., Ghosh, S., 2016. The influence of the El Nino southern oscillation on heat waves in India. Meteorol. Appl. 23 (4), 705–713. https://doi.org/10.1002/met.1594.

Nairn, J., Fawcett, R., Ray, D., 2009. Defining and Predicting Excessive Heat Events, a National System. Cawcr Modelling Workshop.

Nairn, J., Ostendorf, B., Bi, P., 2018. Performance of excess heat factor severity as a global heatwave health impact index. Int. J. Environ. Res. Public Health 15 (11), 26 (Article 2494). https://doi.org/10.3390/ijerph15112494.

Nairn, J.R., Fawcett, R.J.B., 2015. The excess heat factor: a metric for heatwave intensity and its use in classifying heatwave severity. Int. J. Environ. Res. Public Health 12 (1), 227–253. https://doi.org/10.3390/ijerph120100227.

Oueslati, B., Pohl, B., Moron, V., Rome, S., Janicot, S., 2017. Characterization of heat waves in the Sahel and associated physical mechanisms. J. Clim. 30 (9), 3095–3115. https://doi.org/10.1175/jcli-d-16-0432.1.

Parker, T.J., Berry, G.J., Reeder, M.J., Nicholls, N., 2014. Modes of climate variability and heat waves in Victoria, southeastern Australia. Geophys. Res. Lett. 41 (19), 6926–6934. https://doi.org/10.1002/2014gl061736.

Penman, H.L., 1948. Natural evaporation from open water, bare soil and grass. Proc. R. Soc. London 193 (1032), 120–145. https://doi.org/10.1098/rspa.1948.0037.

Perkins, S.E., Alexander, L.V., 2013. On the measurement of heat waves. J. Clim. 26 (13), 4500–4517. https://doi.org/10.1175/jcli-d-12-00383.1.

Perkins, S.E., Alexander, L.V., Nairn, J.R., 2012. Increasing frequency, intensity and duration of observed global heatwaves and warm spells. Geophys. Res. Lett. 39 (5), L20714 https://doi.org/10.1029/2012gl053361.

Perkins, S.E., Argueso, D., White, C.J., 2015. Relationships between climate variability, soil moisture, and Australian heatwaves. J. Geophys. Res.-Atmos. 120 (16), 8144–8164. https://doi.org/10.1002/2015jd023592.

Pettitt, A.N., 1979. A non-parametric approach to the change-point problem. J. R. Stat. Soc.: Ser. C: Appl. Stat. 28 (2), 126–135. https://doi.org/10.2307/2346729, (ISSN: 00359254, 14679876). Publisher: [Wiley, Royal Statistical Society].

Quesada, B., Vautard, R., Yiou, P., Hirschi, M., Seneviratne, S.I., 2012. Asymmetric European summer heat predictability from wet and dry southern winters and springs. Nat. Clim. Chang. 2 (10), 736–741. https://doi.org/10.1038/nclimate1536.

Renwick, J.A., 1998. ENSO-related variability in the frequency of South Pacific blocking. Mon. Weather Rev. 126 (12), 3117–3123. https://doi.org/10.1175/1520-0493(1998)126<3117:Ervitf>2.0.Co;2.

Rex, D.F., 1950. Blocking Action in the Middle Troposphere and its Effect Upon Regional Climate.

Richardson, D., Black, A.S., Irving, D., Matear, R.J., Monselesan, D.P., Risbey, J.S., Squire, D.T., Tozer, C.R., 2022. Global increase in wildfire potential from compound fire weather and drought. Npj Clim. Atmos. Sci. 5 (1), 12 (Article 23). https://doi.org/10.1038/s41612-022-00248-4.

Rowell, D.P., 2009. Projected midlatitude continental summer drying: North America versus Europe. J. Clim. 22 (11), 2813–2833. https://doi.org/10.1175/2008jcli2713.1.

Saji, N.H., Yamagata, T., 2003. Possible impacts of Indian Ocean dipole mode events on global climate. Clim. Res. 25 (2), 151–169. https://doi.org/10.3354/cr025151.

Sang, Y.-F., Singh, V.P., Xu, K., 2019. Evolution of IOD-ENSO relationship at multiple time scales. Theor. Appl. Climatol. 136, 1303–1309. https://doi.org/10.1007/s00704-018-2557-7.

Schumacher, D.L., Keune, J., van Heerwaarden, C.C., de Arellano, J.V.G., Teuling, A.J., Miralles, D.G., 2019. Amplification of mega-heatwaves through heat torrents fuelled by upwind drought. Nat. Geosci. 12 (9), 712–+. https://doi.org/10.1038/s41561-019-0431-6.

Schwingshackl, C., Hirschi, M., Seneviratne, S.I., 2017. Quantifying spatiotemporal variations of soil moisture control on surface energy balance and near-surface air temperature. J. Clim. 30 (18), 7105–7124. https://doi.org/10.1175/jcli-d-16-0727.1.

Seager, R., Hoerling, M., 2014. Atmosphere and ocean origins of North American droughts. J. Clim. 27 (12), 4581–4606. https://doi.org/10.1175/jcli-d-13-00329.1.

Sharma, S., Mujumdar, P., 2017. Increasing frequency and spatial extent of concurrent meteorological droughts and heatwaves in India. Sci. Rep. 7 (9), 15582 https://doi.org/10.1038/s41598-017-15896-3.
Shukla, S., Safeeq, M., AghaKouchak, A., Guan, K., Funk, C., 2015. Temperature impacts on the water year 2014 drought in California. Geophys. Res. Lett. 42 (11), 4384–4393. https://doi.org/10.1002/2015gl063666.
Sun, C., Li, J.P., Ding, R.Q., 2016a. Strengthening relationship between ENSO and western Russian summer surface temperature. Geophys. Res. Lett. 43 (2), 843–851. https://doi.org/10.1002/2015gl067503.
Sun, Q.H., Miao, C.Y., AghaKouchak, A., Duan, Q.Y., 2016b. Century-scale causal relationships between global dry/wet conditions and the state of the Pacific and Atlantic oceans. Geophys. Res. Lett. 43 (12), 6528–6537. https://doi.org/10.1002/2016gl069628.
Sun, Y., Zhang, X.B., Zwiers, F.W., Song, L.C., Wan, H., Hu, T., Yin, H., Ren, G.Y., 2014. Rapid increase in the risk to extreme summer heat in eastern China. Nat. Clim. Chang. 4 (12), 1082–1085. https://doi.org/10.1038/nclimate2410.
Sutanto, S.J., Vitolo, C., Di Napoli, C., D'Andrea, M., Van Lanen, H.A.J., 2020. Heatwaves, droughts, and fires: exploring compound and cascading dry hazards at the pan-European scale. Environ. Int. 134 (9), 15582 https://doi.org/10.1016/j.envint.2019.105276.
Thomas, T., Jaiswal, R.K., Galkate, R.V., Nayak, T.R., 2016. Reconnaissance drought index based evaluation of meteorological drought characteristics in Bundelkhand. Procedia Technol. 24, 23–30. https://doi.org/10.1016/j.protcy.2016.05.005.
Thornthwaite, C.W., 1948. An approach toward a rational classification of climate. Geogr. Rev. 38 (1), 55–94.
Tootle, G.A., Piechota, T.C., 2006. Relationships between Pacific and Atlantic Ocean sea surface temperatures and US streamflow variability. Water Resour. Res. 42 (7), 14 (Article W07411). https://doi.org/10.1029/2005wr004184.
Tootle, G.A., Piechota, T.C., Gutierrez, F., 2008. The relationships between Pacific and Atlantic Ocean sea surface temperatures and Colombian streamflow variability. J. Hydrol. 349 (3–4), 268–276. https://doi.org/10.1016/j.jhydrol.2007.10.058.
Vautard, R., Yiou, P., D'Andrea, F., de Noblet, N., Viovy, N., Cassou, C., Polcher, J., Ciais, P., Kageyama, M., Fan, Y., 2007. Summertime European heat and drought waves induced by wintertime Mediterranean rainfall deficit. Geophys. Res. Lett. 34 (7), 5 (Article L07711). https://doi.org/10.1029/2006gl028001.
Vicente-Serrano, S.M., Begueria, S., Lopez-Moreno, J.I., 2010. A multiscalar drought index sensitive to global warming: the standardized precipitation evapotranspiration index. J. Clim. 23 (7), 1696–1718. https://doi.org/10.1175/2009jcli2909.1.
Wei, J., Wang, W., Shao, Q., Rong, Y., Xing, W., Liu, C., 2019. Influence of mature El Niño-southern oscillation phase on seasonal precipitation and streamflow in the Yangtze River basin, China. Int. J. Climatol. 40 (8), 3885–3905. https://doi.org/10.1002/joc.6433.
Wei, J., Wang, W.G., Shao, Q.X., Yu, Z.B., Chen, Z.F., Huang, Y., Xing, W.Q., 2020. Heat wave variations across China tied to global SST modes. J. Geophys. Res.-Atmos. 125 (6), 22 (Article e2019JD031612). https://doi.org/10.1029/2019jd031612.
Wei, J., Wang, W., Huang, Y., Ding, Y., Fu, J., Chen, Z., Xing, W., 2021. Drought variability and its connection with large-scale atmospheric circulations in Haihe River basin. Water Sci. Eng. 14, 1–16. https://doi.org/10.1016/j.wse.2020.12.007.
Wei, J., Han, W., Wang, W., Zhang, L., Rajagopalan, B., 2023. Intensification of heatwaves in China in recent decades: roles of climate modes. Npj Clim. Atmos. Sci. 6, 98. https://doi.org/10.1038/s41612-023-00428-w.
Wilks, D.S., 1997. Resampling hypothesis tests for autocorrelated fields. J. Clim. 10 (1), 65–82. https://doi.org/10.1175/1520-0442(1997)010<0065:RHTFAF>2.0.CO;2 ((ISSN: 0894-8755, 1520-0442). Publisher: American Meteorological Society Section: Journal of Climate).
Wilks, D.S., 2016. "The stippling shows statistically significant grid points": how research results are routinely overstated and overinterpreted, and what to do about it. Bull. Am. Meteorol. Soc. 97 (12), 2263–2273. https://doi.org/10.1175/BAMS-D-15-00267.1. ISSN: 0003-0007. (Publisher: American Meteorological Society).
Wilks, D.S., 2019. Frequentist statistical inference. In: Wilks, D.S. (Ed.), Statistical Methods in the Atmospheric Sciences, fourth ed. Elsevier, pp. 143–207. https://doi.org/10.1016/B978-0-12-815823-4.00005-5. ISBN: 978-0-12-815823-4. (Chapter 5).
Witte, J.C., Douglass, A.R., da Silva, A., Torres, O., Levy, R., Duncan, B.N., 2011. NASA A-train and Terra observations of the 2010 Russian wildfires. Atmos. Chem. Phys. 11 (17), 9287–9301. https://doi.org/10.5194/acp-11-9287-2011.
Wong, G., van Lanen, H.A.J., Torfs, P.J.J.F., 2013. Probabilistic analysis of hydrological drought characteristics using meteorological drought. Hydrol. Sci. J. 58 (2), 253–270. https://doi.org/10.1080/02626667.2012.753147.
Wu, X.Y., Hao, Z.C., Hao, F.H., Li, C., Zhang, X., 2019a. Spatial and temporal variations of compound droughts and hot extremes in China. Atmosphere 10 (2), 10 (Article 95). https://doi.org/10.3390/atmos10020095.
Wu, X.Y., Hao, Z.C., Hao, F.H., Zhang, X., 2019b. Variations of compound precipitation and temperature extremes in China during 1961-2014. Sci. Total Environ. 663, 731–737. https://doi.org/10.1016/j.scitotenv.2019.01.366.
Wu, X.Y., Hao, Z.C., Hao, F.H., Zhang, X., Singh, V.P., Sun, C., 2021a. Influence of large-scale circulation patterns on compound dry and hot events in China. J. Geophys. Res.-Atmos. 126 (4), 15 (Article e2020JD033918). https://doi.org/10.1029/2020jd033918.
Wu, X.Y., Hao, Z.C., Tang, Q.H., Zhang, X., Feng, S.F., Hao, F.H., 2021b. Population exposure to compound dry and hot events in China under 1.5 and 2 degrees C global warming. Int. J. Climatol. 41 (12), 5766–5775. https://doi.org/10.1002/joc.7152.
Xu, F., Luo, M., 2019. Changes of concurrent drought and heat extremes in the arid and semi-arid regions of China during 1961-2014. Atmos. Sci. Lett. 20 (12), 10 (Article e947). https://doi.org/10.1002/asl.947.
Yang, Q., Ma, Z.G., Fan, X.G., Yang, Z.L., Xu, Z.F., Wu, P.L., 2017. Decadal modulation of precipitation patterns over eastern China by sea surface temperature anomalies. J. Clim. 30 (17), 7017–7033. https://doi.org/10.1175/jcli-d-16-0793.1.
Ye, L., Shi, K., Xin, Z.H., Wang, C., Zhang, C., 2019. Compound droughts and heat waves in China. Sustainability 11 (12), 14 (Article 3270). https://doi.org/10.3390/su11123270.
Yuan, W.P., Cai, W.W., Chen, Y., Liu, S.G., Dong, W.J., Zhang, H.C., Yu, G.R., Chen, Z.Q., He, H.L., Guo, W.D., Liu, D., Liu, S.M., Xiang, W.H., Xie, Z.H., Zhao, Z.H., Zhou, G.M., 2016. Severe summer heatwave and drought strongly reduced carbon uptake in southern China. Sci. Rep. 6 (12), 18813 https://doi.org/10.1038/srep18813.
Zampieri, M., Ceglar, A., Dentener, F., Toreti, A., 2017. Wheat yield loss attributable to heat waves, drought and water excess at the global, national and subnational scales. Environ. Res. Lett. 12 (6), 11 (Article 064008). https://doi.org/10.1088/1748-9326/aa723b.
Zhang, B.Q., Wang, Z.K., Chen, G., 2017b. A sensitivity study of applying a two-source potential evapotranspiration model in the standardized precipitation evapotranspiration index for drought monitoring. Land Degrad. Dev. 28 (2), 783–793. https://doi.org/10.1002/ldr.2548.
Zhang, J., Liu, Z.Y., Chen, L., 2015. Reduced soil moisture contributes to more intense and more frequent heat waves in northern China. Adv. Atmos. Sci. 32 (9), 1197–1207. https://doi.org/10.1007/s00376-014-4175-3.
Zhang, L.Y., Zhang, Z., Ye, T., Zhou, M.G., Wang, C.Z., Yin, P., Hou, B., 2018. Mortality effects of heat waves vary by age and area: a multi-area study in China. Environ. Health 17 (12), 54. https://doi.org/10.1186/s12940-018-0398-6.
Zhang, Q., Kong, D.D., Singh, V.P., Shi, P.J., 2017a. Response of vegetation to different time-scales drought across China: spatiotemporal patterns, causes and implications. Glob. Planet. Chang. 152, 1–11. https://doi.org/10.1016/j.gloplacha.2017.02.008.
Zhang, Y., Hao, Z., Feng, S., Zhang, X., Hao, F., 2022. Changes and driving factors of compound agricultural droughts and hot events in eastern China. Agric. Water Manag. 263 https://doi.org/10.1016/j.agwat.2022.107485.
Zhou, P., Liu, Z.Y., 2018. Likelihood of concurrent climate extremes and variations over China. Environ. Res. Lett. 13 (9), 10 (Article 094023). https://doi.org/10.1088/1748-9326/aade9e.
Zscheischler, J., Seneviratne, S.I., 2017. Dependence of drivers affects risks associated with compound events. *Science*. Advances 3 (6), 10 (Article e1700263). https://doi.org/10.1126/sciadv.1700263.
Zscheischler, J., Westra, S., van den Hurk, B., Seneviratne, S.I., Ward, P.J., Pitman, A., AghaKouchak, A., Bresch, D.N., Leonard, M., Wahl, T., Zhang, X.B., 2018. Future climate risk from compound events. Nat. Clim. Chang. 8 (6), 469–477. https://doi.org/10.1038/s41558-018-0156-3.

Dataset references

National, M, 2019. Daily Meteorological Dataset of Basic Meteorological Elements of China National Surface Weather Station (V3.0)(1951-2010). National Tibetan Plateau/Third Pole Environment Data Center.
Rayner, N.A., Parker, D.E., Horton, E.B., Folland, C.K., Alexander, L.V., Rowell, D.P., Kent, E.C., Kaplan, A., 2003. Global analyses of sea surface temperature, sea ice, and night marine air temperature since the late nineteenth century. J. Geophys. Res. 108 (D14), 4407. https://doi.org/10.1029/2002JD002670.
Huang, Boyin, Thorne, Peter W., Banzon, Viva F., Boyer, Tim, Chepurin, Gennady, Lawrimore, Jay H., Menne, Matthew J., Smith, Thomas M., Vose, Russell S., Zhang, Huai-Min, 2017. NOAA Extended Reconstructed Sea Surface Temperature (ERSST), Version 5. NOAA National Centers for Environmental Information. https://doi.org/10.7289/V5T72FNM (Obtain at NOAA/ESRL/PSD at their website https://www.esrl.noaa.gov/psd/).